JGR Solid Earth

RESEARCH ARTICLE
10.1029/2025JB031692

Present-Day Kinematics and Seismic Hazards in Turkey: Insights From a TVR-Optimized Block Model and High-Resolution GNSS Strain Rates

Kai Sun[1,2], Wenbin Xu[1,2], Qijie Wang[1,2], Lei Xie[1,2], Guojie Meng[3], and Lijia He[4]

[1]School of Geoscience and Info-Physics, Central South University, Changsha, China, [2]Key Laboratory of Metallogenic Prediction of Nonferrous Metals and Geological Environment Monitoring Ministry of Education, Changsha, China, [3]Key Laboratory of Earthquake Forecasting, China Earthquake Administration, Beijing, China, [4]Earth Observatory of Singapore, Nanyang Technological University, Singapore, Singapore

Key Points:

- We develop a total variation regularization optimized block model for Turkey using dense Global Navigation Satellite System data
- We describe the heterogeneous slip partitioning and deformation mechanisms driven by inter and intra-plate interactions across Turkey
- We quantify the on-fault and off-fault moment accumulation rates across Turkey

Supporting Information:

Supporting Information may be found in the online version of this article.

Correspondence to:

W. Xu,
wenbin.xu@csu.edu.cn

Citation:

Sun, K., Xu, W., Wang, Q., Xie, L., Meng, G., & He, L. (2026). Present-day kinematics and seismic hazards in Turkey: Insights from a TVR-optimized block model and high-resolution GNSS strain rates. *Journal of Geophysical Research: Solid Earth*, *131*, e2025JB031692. https://doi.org/10.1029/2025JB031692

Received 28 MAR 2025
Accepted 2 APR 2026

Author Contributions:

Conceptualization: Kai Sun, Wenbin Xu, Lei Xie, Guojie Meng
Funding acquisition: Wenbin Xu, Qijie Wang
Methodology: Kai Sun, Wenbin Xu, Lei Xie, Lijia He
Project administration: Wenbin Xu
Software: Kai Sun
Supervision: Wenbin Xu, Qijie Wang
Validation: Kai Sun, Wenbin Xu, Qijie Wang, Guojie Meng
Visualization: Kai Sun, Lei Xie
Writing – original draft: Kai Sun
Writing – review & editing: Wenbin Xu, Qijie Wang, Guojie Meng, Lijia He

Abstract Turkey, at the intersection of Eurasian, Arabian, and African plates, is characterized by spatially heterogeneous fault behavior and experiences frequent destructive earthquakes. Here, we systematically investigate present-day kinematics and seismic hazards in Turkey using dense Global Navigation Satellite System observations. We construct an objective block model using total variation regularization after building an initial model integrating multi-source data sets. Our model quantifies slip partitioning in the active fault systems (e.g., 6.3 vs. 3.1 mm/yr between main and secondary branches of the East Anatolian fault zone) and determines slip rates along geodetically identified tectonic boundaries (e.g., 4.0 ± 0.4 mm/yr contraction rate on the Tercan fault). Concurrently, we calculate continuous strain-rate field that reveals the concentrated (e.g., North Anatolian fault zone [NAFZ]) and distributed strain (e.g., northeastern Turkey) across Turkey, as well as intra-plate tectonic transforms (e.g., notable compression along the Eldivan-Elmadağ Pinched Crustal Wedge [EPCW]). The contraction along the EPCW appears linked to localized stress rotation and large bending of the NAFZ under long-term Anatolian extrusion. Additionally, we find no geodetic evidence supporting two previously proposed intraplate escape pathways: a strike-slip system between the eastern Anatolian shear zone, Antalya-Kekova fault zone, and Pliny-Strabo shear zone (PSSZ), or a linkage between the Fethiye-Burdur fault zone and PSSZ. Furthermore, using fault slip-rates and block internal strain-rates, we calculate on-fault and off-fault moment accumulation rates across Turkey. We find close agreement between cumulative geodetic and seismic moments, with sustained lower seismic rates relative to accumulation rates suggesting elevated potential for major earthquakes.

Plain Language Summary The Anatolian region frequently experiences destructive earthquakes, such as the devastating 2023 Turkey Mw 7.8 and 7.5 events, highlighting the importance of understanding how the land deforms and accumulates stress. Using space geodetic data, we identify faults with detectable deformation across Turkey and develop a model to estimate their motion rates. Our findings reveal that some major faults individually absorb the vast majority of motion between tectonic plates, while some faults participate through multi-branched or distributed parallel structures. Additionally, fault motions differ across Turkey, similar to how earthquake patterns vary regionally. Our calculations show that the annual energy accumulation on major faults is equivalent to a magnitude 6.9 earthquake, and the total estimated energy accumulation since 1900 broadly matches the actual seismic energy release. When the seismic moment release rate is comparable to the geodetically inferred moment accumulation rate, the likelihood of major earthquakes is low; conversely, a persistently lower release rate indicates elevated seismic hazard. These findings demonstrate the value of incorporating ground deformation measurements into seismic hazard assessment for fault systems in Turkey, and further development of advanced probabilistic seismic hazard models incorporating long-term earthquake catalogs is essential.

1. Introduction

The plate tectonic framework of the lithosphere beneath Turkey is characterized by the continental collision of the Eurasian and Arabian plates in the northeast and subduction of the African oceanic lithosphere in the south and west (McKenzie, 1970, 1972). Due to the ongoing Arabia-Eurasia convergence and Aegean slab rollback, the Anatolian microplate is escaping westward along two major strike-slip boundaries (Figure 1a; e.g., Dewey & Şengör, 1979; Faccenna et al., 2006; Reilinger et al., 1997; Şengör, 1979). The North Anatolian Fault Zone

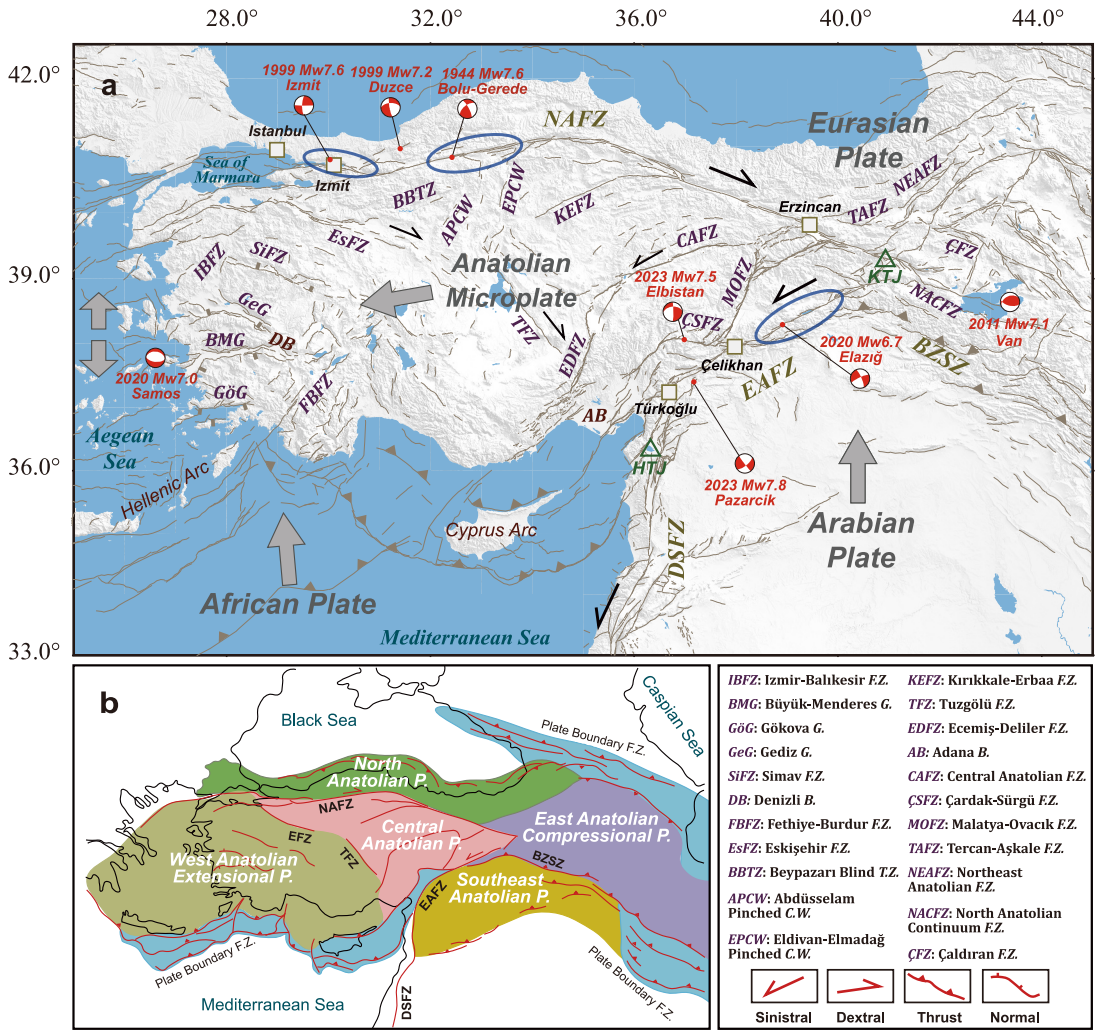

Figure 1. (a) Tectonic setting of Turkey and surrounding regions. Active fault traces are from Zelenin et al. (2022) and Seyitoglu et al. (2022b). Blue ellipses indicate creeping segments identified by Hussain et al. (2018) and Çakir et al. (2023) using Interferometric Synthetic Aperture Radar observations. Focal mechanisms are sourced from the Global Centroid Moment Tensor catalog (https://www.globalcmt.org/) and Eyidogan et al. (1991) (the 1944 Mw 7.6 Bolu-Gerede earthquake). Abbreviations: NAFZ, North Anatolian Fault Zone; EAFZ, East Anatolian Fault Zone; BZSZ, Bitlis-Zagros Suture Zone; DSFZ, Dead Sea Fault Zone; KTJ, Karlıova Triple Junction; and HTJ, Hatay Triple Junction. Other abbreviations are shown in the inset figure at bottom right. (b) Neotectonic provinces of Turkey (Emre et al., 2018; Seyitoglu et al., 2022a). Province and Fault Zone are abbreviated as "P." and "F.Z.", respectively. Additional abbreviations: EFZ, Eskişehir Fault Zone; TFZ, Tuzgölü Fault Zone.

(NAFZ) formed by ca. 15-11 Ma near Erzincan and propagated westward (e.g., Armijo et al., 1999; Şengör et al., 2005), with the East Anatolian Fault Zone (EAFZ) developed at ca. 5 Ma, marking the creation of the Anatolian microplate (e.g., Hempton, 1987; Whitney et al., 2023). Concurrently, complex interactions between and within plates give rise to various fault systems and faulting styles across Anatolia under heterogeneous stresses and time-varying tectonic conditions (Figure 1b; e.g., Aktug et al., 2009, 2013a; Esat et al., 2021; Mozafari et al., 2019; Van Hinsbergen et al., 2016; Whitney et al., 2023; Şengör et al., 2005). Consequently, the Turkish region frequently experiences devastating earthquakes with diverse rupture mechanisms, causing catastrophic damage and heavy casualties (Figure 1a; Bikçe, 2016). This pronounced seismic risk, driven by ongoing tectonic activities, necessitates present-day kinematic studies and seismic hazard assessment across the region.

Starting with the earliest Global Positioning System (GPS) studies that provided evidence for Anatolia-Eurasia decoupling (e.g., Burc Oral et al., 1995; Straub & Kahle, 1994), measurements from Global Navigation Satellite System (GNSS) have progressively revealed multi-scale kinematic patterns across Anatolia over the past three decades (e.g., Aktug et al., 2009; Esat et al., 2021; McClusky et al., 2000; Reilinger et al., 2006; Seyitoglu

et al., 2022a). Broad-scale GNSS campaigns have constrained relative motions between adjacent plates and upper-bound slip rates along major boundary faults (i.e., NAFZ and EAFZ) in earlier studies (e.g., McClusky et al., 2000; Reilinger et al., 1997). The first-order velocity variations across Turkey have been further quantified through tectonic block modeling (e.g., Nyst & Thatcher, 2004; Reilinger et al., 2006). In general, the vast majority of the Turkish region rotates counterclockwise relative to Eurasia, with velocities increasing east-to-west from ∼15 mm/yr in the Arabian plate to ∼21 mm/yr in the Anatolian microplate, and reaching ∼33 mm/yr in the Aegean microplate. This differential motion is primarily accommodated by 20–30 mm/yr of dextral strike-slip rate on the NAFZ, ∼10 mm/yr of sinistral strike-slip on the EAFZ, and ∼20 mm/yr of extension across the graben systems in western Turkey (Reilinger et al., 2006).

With the widespread application of regional-scale GNSS networks and Interferometric Synthetic Aperture Radar (InSAR) techniques, along-fault variations in slip rates and complex deformation patterns across distinct tectonic units have been investigated (e.g., Aktug et al., 2009, 2013a, 2013b, 2016; Barbot & Weiss, 2021; Cavalié & Jónsson, 2014; Esat et al., 2021; Gezgin et al., 2022; Hussain et al., 2018; Özbey et al., 2021; Özkan et al., 2023). For instance, along the NAFZ, InSAR reveals a westward slip-rate increase from ∼22 mm/yr at the Karlıova Triple Junction (KTJ) to ∼30 mm/yr near Istanbul (Figure 1a; Hussain et al., 2018). Continuing westward to the Sea of Marmara, GNSS-constrained block model revealed that lateral motion is partitioned to ∼25 mm/yr on the northern branch and 3–6 mm/yr on the southern branch (Aktug et al., 2009). In central Turkey, the Central Anatolian Fault Zone (CAFZ) exhibits sinistral strike-slip rate of ∼1 mm/yr, while the Tuzgölü and Eskişehir fault zones act as tectonic boundaries separating the Central Anatolian Province and West Anatolian Extensional Province, exhibiting dextral strike-slip rates of ∼2–5 mm/yr and ∼1–6 mm/yr, respectively, as derived from GNSS block models (Aktug et al., 2013a; Esat et al., 2021; Gezgin et al., 2022). Further west, extensional deformation is distributed across graben systems, with the Denizli Basin showing the highest extension rate of ∼8–13 mm/yr (Aktug et al., 2009; Reilinger et al., 2006). GNSS-constrained kinematic modeling and the latest InSAR velocity field indicate that continuous deformation models or block models incorporating sufficient structures can effectively interpret surface velocity changes in western Turkey (Aktug et al., 2009; Diercks et al., 2024).

The progressive accumulation of GNSS data across Turkey has now produced a data set of sufficient density and longevity that resolves deformation across scales, from plate-boundary motions down to localized strain (Ergintav et al., 2023; Seyitoglu et al., 2022a). Using densified GNSS observations and a simplified block model, Ergintav et al. (2023) analyzed the concentrated and distributed strain across Anatolia under active plate interactions. By developing a complex block model based on focal mechanisms, satellite imagery, and pseudo-tectonic (geologically meaningless) boundaries to interpret the GNSS velocity field from Kreemer et al. (2014), Seyitoglu et al. (2022a) refined the delineation of neotectonic provinces in Turkey (e.g., Anatolian Diagonal Shear Province).

Nevertheless, in the process of gradually deciphering Anatolian kinematics, some regions exhibit unresolved disagreements between geodetic solutions and geological investigations or seismicity levels. For instance, geodetic modeling generally simplifies the southwestern section of the EAFZ to a single fault, estimating an integrated slip rate of ∼10 mm/yr, while geological estimates indicate that there is a significant slip-rate partitioning, with the main and secondary branches of the EAFZ absorbing 2/3 (∼6 mm/yr) and 1/3 (∼3 mm/yr), respectively (Duman & Emre, 2013). Özbey et al. (2024) resolved this controversy by incorporating the Malatya-Çardak fault as a block boundary, which is structurally inconsistent with the geologically mapped secondary branch of the EAFZ. Similarly, block models around the KTJ commonly interpret the northern extension of the EAFZ as the boundary of the East Anatolian compressional zone, conflicting with geological evidence that suggests a more westerly boundary (Temiz et al., 2002; Şahin et al., 2019). These models also overlook the eastern continuation of the NAFZ, where significant seismic activity occurs. In contrast, in northwestern Central Anatolia, Esat et al. (2021) developed a dense block model constrained by GNSS data, revealing remarkably high compression rates (>10 mm/yr) across the Eldivan-Elmadağ Pinched Crustal Wedge (EPCW) that strikingly contrast with the regional low seismicity. Furthermore, in systematic kinematic modeling of Anatolia, Ergintav et al. (2023) oversimplified by not incorporating certain structures now known to be seismogenic, such as the fault that generated the 2023 Mw 7.5 Elbistan earthquake (Figure 1a). Meanwhile, the overly complex model of Seyitoglu et al. (2022a) produces some results that diverge from field observations, such as strike-slip direction along the Tuzgölü and Eskişehir faults.

In this study, we aim to reconcile these inconsistencies and systematically investigate present-day kinematics and seismic hazards across Turkey through an objectively constrained block model based on dense GNSS observations. By integrating modeling strategies from previous studies, active fault database, and compiled earthquake catalog, we construct an initial complex model. The total variation regularization (TVR) method is then applied to optimize the model by eliminating boundaries lacking detectable strain localization. Furthermore, we complement the block model with strain-rate fields to explore heterogeneous kinematics and deformation mechanisms. Finally, by combining fault slip rates with block-internal strain, we quantify both on-fault and off-fault moment accumulation rates across Turkey and compare them with seismic moment release from earthquake catalogs.

2. Data

2.1. GNSS Velocity Field

We adopt the velocity field from Kurt et al. (2023) for kinematic analysis due to its unprecedented spatial density. This data set is compiled from various research projects, including "The Turkish National Fundamental GPS Network" (TNFGN; 608 stations), "The Turkish Real-Time Kinematic GNSS Network" (CORS-TR; 134 stations), and others (e.g., Turkish National Permanent GNSS Network, TNPGN), totaling 836 stations (Kurt et al., 2023). The data set covers the period from 1992 to 2020, with varying observation durations and modes across sites. All data are processed using homogeneous time series analysis, with uncertainties derived from a first-order Gauss-Markov noise model, and referenced to a fixed Eurasian reference frame. For time series in which earthquake events exist, only pre-earthquake observations are used to derive velocity solutions. Notably, whether the observed deformation along the prominent creeping segment of NAFZ reflects long-term postseismic effects or motion sustained over multiple seismic cycles remains unclear (e.g., Bilham et al., 2016; Hussain et al., 2016; Jolivet et al., 2023). We will specifically account for these signals in subsequent kinematic modeling. To further refine the block model constraints, sparse observations on Aegean Sea islands and anomalies are removed, while 19 additional observations from Karakhanyan et al. (2013) and Djamour et al. (2011) in northeastern Turkey are incorporated. These additional observations are unified in reference by removing rotation components derived from residuals of common sites with the original velocity field. For spatially overlapping stations, those with longer observational time spans are retained.

Compared to the velocity field of Kurt et al. (2023), Ergintav et al. (2023) provided a sparser velocity solution yet with reliable uncertainties using maximum likelihood estimation under a white-plus-flicker noise model (Santamaría-Gómez et al., 2011; Williams et al., 2004). We therefore correct the uncertainties in Kurt et al. (2023) by calculating the median differences in uncertainty at common stations between the two data sets, applying scaling factors of 4.6 and 4.4 to the east and north components, respectively (Figure S1 in Supporting Information S1; e.g., Wang et al., 2022). Meanwhile, to compensate for epistemic errors neglected in the uncertainty estimation, we introduce an ad hoc minimum uncertainty σ_m to re-estimate the uncertainties of horizontal components σ_i:

$$\sigma_i' = \left(\sigma_m{}^2 + \sigma_i{}^2\right)^{1/2} \tag{1}$$

σ_i represents the original uncertainty; σ_m is assigned a value of 0.3 (e.g., Shen & Bird, 2022). This step also ensures robust data weighting in kinematic inversion (e.g., Hammond et al., 2024). After quality control removing observations above the 95th percentile uncertainty limit, the final GNSS velocity field contains 792 stations.

Figure 2a displays the velocity field with respect to the fixed Eurasian plate. The GNSS velocity vectors clearly show the counterclockwise westward escape of the Anatolian microplate, with distinct velocity gradients and rotations localized along plate boundaries.

2.2. Earthquake Catalog

Significant efforts have been made in previous studies to digitize and homogenize historical and instrumental records, resulting in accessible databases of seismological observation products for Turkey (Stucchi et al., 2013; Tan, 2021; Tan et al., 2008). Considering the limitations in parameter accuracy and catalog completeness of historical earthquake records, only modern instrumental catalogs (1900–2025) are used in this study. We use two modern earthquake databases: the "Turkish Homogenized Earthquake Catalog" (Turkish Homogenized Earthquake Catalogue (TURHEC), 1900–June 2021, Tan, 2021) and data from the Disaster and Emergency

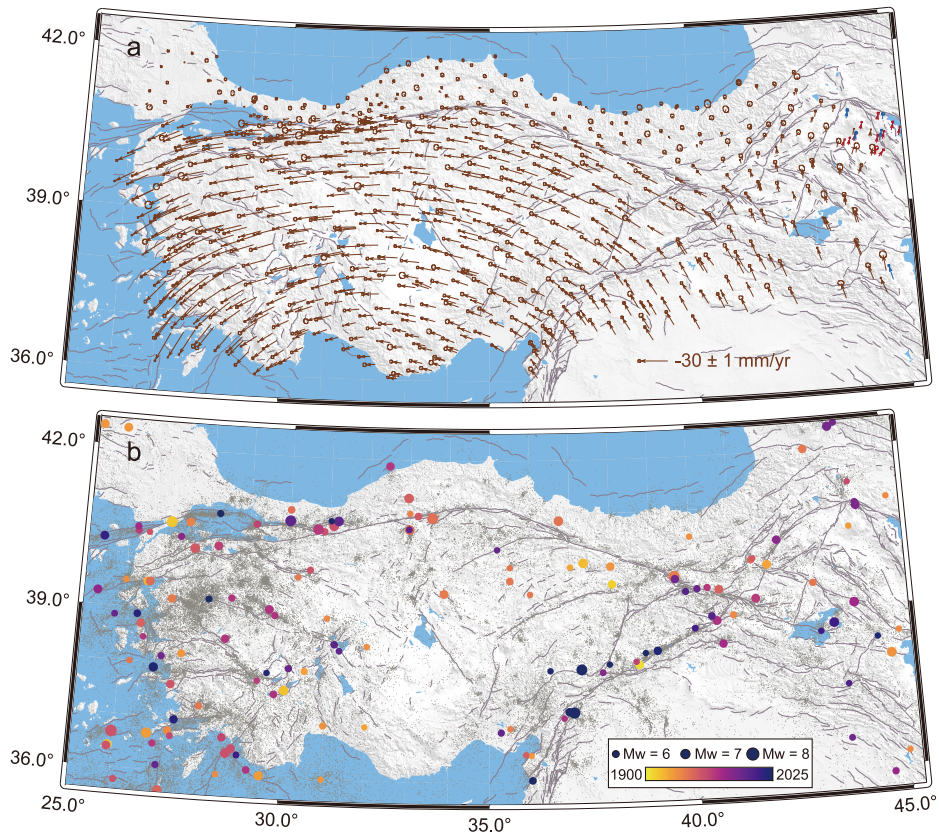

Figure 2. (a) Global Navigation Satellite System horizontal velocities with 95% confidence levels relative to the fixed Eurasian plate. Brown, red, and blue velocity vectors represent data from Kurt et al. (2023), Karakhanyan et al. (2013), and Djamour et al. (2011), respectively. (b) Compiled earthquake catalog spanning 1900 to 2025. Gray dots show earthquakes with Mw < 5.9, while colored dots denote events of Mw ≥ 5.9. Solid gray lines represent active faults (Zelenin et al., 2022).

Management Authority (AFAD, July 2021–August 2025), to compile the entire earthquake catalog. We convert local magnitude and surface-wave magnitude in the AFAD catalog to equivalent moment magnitude using empirical linear relations in Tan (2021) (Table S1 in Supporting Information S1). Then, the combined earthquake catalog is declustered using the technique proposed by Gardner & Knopoff (1974) to ensure the data conforms to a Poisson distribution. Records exceeding the maximum crustal thickness (~50 km) are excluded (Akin, 2016). Possible artificial events with magnitudes below 2.5 are also removed. In the end, 76,459 earthquake events are retained. The compiled catalog exhibits a magnitude of completeness of Mw 5.9 (Figure S2 in Supporting Information S1). Figure 2b displays the spatial distribution of earthquakes between 35.4°N and 42.7°N and 25.0°E–45.3°E, where the locations of major earthquakes show first-order correlation with active tectonic structures and fault systems.

3. Model and Methodology

3.1. Block Modeling

In the block modeling approach, we assume that active fault zones accumulate most of the tectonic deformation in the region. An interconnected network of faults is used to form a series of quasi-rigid blocks. By simultaneously quantifying block motions and slip rates of faults acting as boundaries, we can capture large-scale kinematic characteristics in a systematic manner. In this context, objective and appropriate determination of block boundaries and fault geometry parameters is essential.

3.1.1. Determination of Initial Block Boundaries

In this stage, we integrate multi-source observations to construct a set of boundaries for generating an initial block model. Our modeling synthesizes strategies from previous studies, active fault database, and compiled earthquake catalog, which can be organized into three steps as follows.

In the first step, we construct the preliminary block model referring to previous studies. In western Anatolia, we define four approximately E-W-oriented boundaries corresponding to the Simav fault zone, Gediz graben, Büyük Menderes graben, and Gökova graben, following Aktug et al. (2009). Additionally, the western Izmir-Balıkesir fault zone (Solak et al., 2024) and the eastern Fethiye-Burdur fault zone (FBFZ; Aktug et al., 2009; Tiryakioğlu et al., 2013) form approximately NE-SW-trending boundaries (Figure 1a). East of the FBFZ, a symmetric boundary is incorporated to delineate the Isparta Angle (Tiryakioğlu et al., 2013). In northern Anatolia, block boundaries are modeled based on the NAFZ and its two branches in the Sea of Marmara (Reilinger et al., 2006). In north Central Anatolia, we define a triangle-shaped block bounded by the Eskişehir fault zone and the Kırıkkale-Erbaa fault zone according to Esat et al. (2021). This block is further subdivided into three sub-blocks based on the intermittent traces of the EPCW and Beypazari blind thrust zone (Esat et al., 2021). The Abdüsselam pinched crustal wedge is not treated as a separate boundary due to its proximity to the EPCW. To the east, we extend a block bounded by the Tuzgölü fault zone, CAFZ, and a portion of the NAFZ. The boundary along the CAFZ extends southwestward to the Ecemiş-Deliler fault zone (Aktug et al., 2013a). The main branch of the EAFZ is modeled as the boundary between the Anatolian microplate and the Arabian plate. In northeastern Turkey, block boundaries are primarily defined along the Bitlis-Zagros Suture Zone (BZSZ), the Çaldıran fault zone, and the northeastern extension of the EAFZ (Djamour et al., 2011; Reilinger et al., 2006). The Lesser Caucasus region is further subdivided into three smaller blocks following Karakhanyan et al. (2013).

In the second step, we align the surface strikes and nodes of active faults with geological field observations based on the active fault database of Zelenin et al. (2022). The fault database of Zelenin et al. (2022) in Turkey is a compilation of a series of databases, mainly from Emre et al. (2013) and Basili et al. (2013). For instance, we reorient the block boundaries in western Turkey to correspond with the principal boundaries of the graben systems. Additionally, we introduce extra block boundaries based on fault traces, such as secondary structures in southeastern Turkey, including the Sürgü-Çardak-Savrun fault zone and the Malatya-Ovacık fault zone. Several segments of these block boundaries were ruptured during the 2023 earthquake doublet (Reitman et al., 2023).

In the third step, we further adjust the block boundaries with reference to the earthquake catalog and add the necessary seismogenic faults as boundaries. For example, from a series of NE-SW trending parallel fault zones in northeastern Turkey, we select the segment with the highest seismicity as the northeastern extension of the EAFZ. Additionally, we incorporate the Tercan fault and the North Anatolian Continuum fault zone as additional block boundaries, allowing the complex deformation and frequent seismic activity around the KTJ to be interpreted through the relative motions of four adjacent tectonic blocks (Figure 1a). Besides, we introduce an N-S oriented boundary within the Isparta Angle block, aligned with local linear seismicity (Nissen et al., 2022).

It should be noted that, considering potential location biases in the active fault database and earthquake catalog, we validate the fit of near-field GNSS data across faults during each boundary adjustment in the second and third steps. In cases of conflicting data sets, we prioritize solutions consistent with GNSS observations. Accordingly, the study area is tectonically separated into 25 blocks as shown in Figure 3.

3.1.2. Determination of Fault Dip and Locking Depth

The updated active fault database in Turkey provides referenceable fault dip records obtained from field surveys, digital terrain analysis, and aerial photo interpretations (Emre et al., 2018; Zelenin et al., 2022). This information allows us to appropriately determine the dip angles of the block boundaries with compressional and extensional structures (Table S2 in Supporting Information S1). For boundaries that have the same dip direction but differ in dip angles along the strike, an average dip is assigned.

To determine the optimal locking depth, we use both residual statistics estimation and seismic cutoff depth methods. Initially, based on the studies of Hussain et al. (2018) and Bletery et al. (2020), we preset the locking depths of the central and eastern segments of the NAFZ (from İzmit to the KTJ) and the northeastern segment of the EAFZ (from Çelikhan to the KTJ) to 16 and 5 km, respectively. For creeping segments on both faults, enforcing shallow locking or full creep in simplified block model proved ineffective (Figure S3 in Supporting

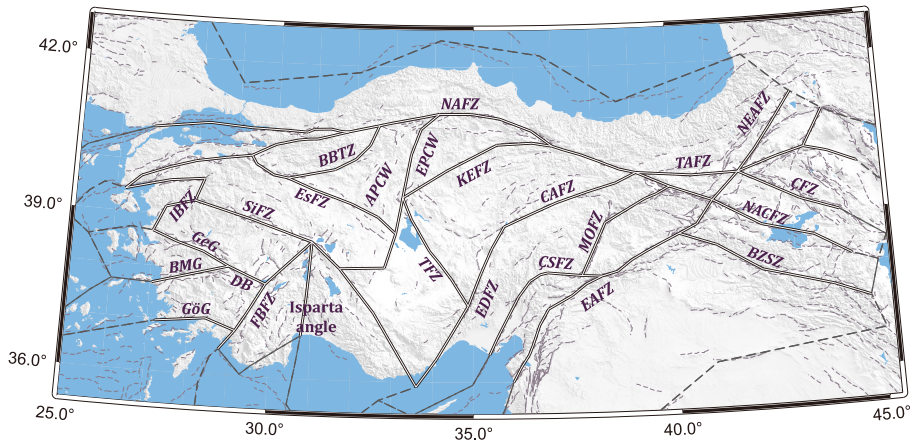

Figure 3. The initial block model constructed for Turkey. Solid black lines indicate block boundaries that follow reliable geological and geophysical evidence, and dashed brown lines indicate fault segments and pseudo boundaries outside Turkey. Abbreviations in this figure are consistent with those in Figure 1.

Information S1). We thus adopt the same locking depths as adjacent segments, then remove outliers affected by creep after the first inversion. For the outermost bounding faults of tectonic blocks, the locking depth is set to 0 km, indicating free-slip conditions without strain accumulation. We then systematically evaluate the Root Mean Square of residuals by varying the locking depth of other faults from 0 to 40 km in 1 km increments to search for the global optimal locking depth. Concurrently, we calculate the 90% and 95% cut-off depths of earthquakes. The optimal locking depth derived from residual statistics is 12 km, slightly shallower than the 90% cutoff depth of 15 km (Figure 4a).

A uniform locking depth of 15 or 16 km was assumed in previous block models based on earthquake catalogs (Ergintav et al., 2023; Seyitoglu et al., 2022a). To address the discrepancy between the residual-based locking depth and seismic cutoff depth, as well as to explore spatial variations of the seismogenic depth across Turkey, we divide Turkey into eastern and western parts at ∼33°E. We first fixed the locking depth of faults in western Turkey to the globally optimal value of 12 km and then re-estimated the optimal locking depth for eastern Turkey, obtaining 18 km (Figure 4b). Subsequently, we set the locking depth of faults in eastern Turkey to 18 km and re-evaluated the optimal locking depth for western Turkey, determining a shallower estimate of 9 km (Figure 4c). The resulting east-to-west decrease in locking depth (18–9 km) from residual statistics agrees well with documented lithospheric evolution and crustal thickness variations (Akin, 2016; England et al., 2016). In contrast, the 90% seismic cutoff depth remains consistently around 15 km across all regions, likely constrained by the level of instrumental accuracy or station density rather than true variations in seismogenic layer thickness (Figure 4).

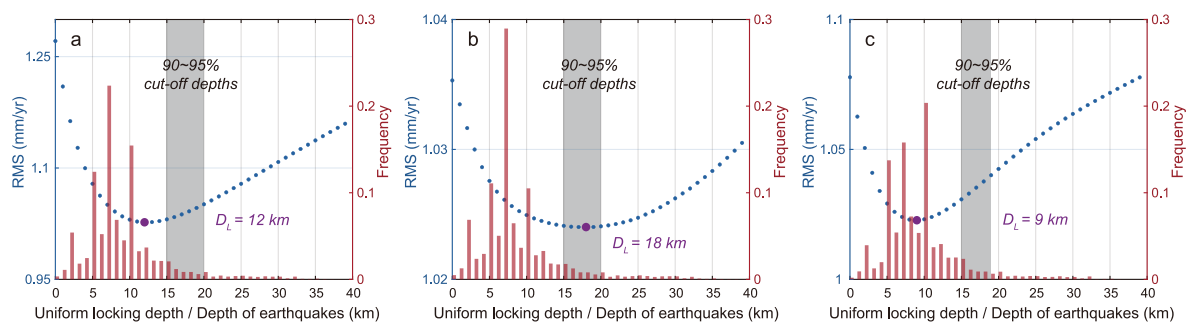

Figure 4. Optimal locking depths determined from earthquake catalogs and residual statistics in (a) the entire Turkey, (b) eastern Turkey, and (c) western Turkey. The histograms show the frequency distributions of the focal depths of earthquakes, with the dashed lines representing the 90% and 95% cut-off depths. The circles show the variations of Root Mean Square with the locking depths, and the purple circles indicate the optimal locking depths D_L.

3.1.3. TVR-Optimized Block Model and Model Inversion

Assuming that the GNSS measurements are quasistatic nominally inter-seismic velocities, the velocity V_I can be defined as:

$$V_I = V_B + V_E + V_R \tag{2}$$

where V_B and V_E represent the surface velocities corresponding to block rotation and elastic strain accumulation on faults, respectively (Meade & Loveless, 2009). V_R represents residual velocity, reflecting the misfit between observation and model prediction. In certain instances, the misfit may indicate activity of secondary structures or unmodeled complex tectonic deformation (e.g., Wang et al., 2021).

The forward problem is further formulated as:

$$V_I = \mathrm{Gm} + V_R = [G_B - G_E]\Omega + V_R \tag{3}$$

in which G_B represents coordinate and geometric conversions between Euler vectors Ω and surface velocity components, G_E combines the partial derivative matrix of elastic Green's functions (Okada, 1985) with the projection matrix converting block-differential motions to fault-slip components.

The inverse problem can be solved in a weighted least squares sense:

$$m_{\mathrm{est}} = \left(G^T W G\right)^{-1} G^T W d \tag{4}$$

W is the weighting matrix constructed from the GNSS velocity uncertainties. d is the observation matrix of GNSS horizontal components.

The TVR strategy automatically filters out inactive structures by grouping blocks with similar rotation vectors (e.g., Evans, 2022; Evans et al., 2015; Huang & Evans, 2019). Specifically, we simultaneously minimize the L_2-norm of data residuals and the L_1-norm of rotation differences between adjacent blocks:

$$\min\left(W^{\frac{1}{2}}\|\mathrm{Gm} - d\|_2 + \lambda\|\mathrm{Dm}\|_1\right) \tag{5}$$

in which λ governs the strength of the regularization term, and D is a linear operator characterizing block adjacency. The minimization in Equation 5 is performed using the convex optimization solver CVX (Grant & Boyd, 2008, 2013). Note that TVR is employed solely to provide boundary retention references and is excluded from the final inversion. In applying the algorithm, we divide Turkey into three overlapping regions to enable cross-validation of the results (Figure S4 in Supporting Information S1).

3.2. Continuous Strain Rate Field Derivation From Discrete GNSS Velocities

We use GNSS velocity vectors to calculate the strain rates and associated standard errors following the method of Shen et al. (2015). To ensure spatial continuity of the strain rate field, aseismic creep observations previously excluded during block modeling are reintegrated into the data set. The continuous strain-rate field is obtained by spatially weighted inversion of discrete GNSS horizontal components in a weighted least-squares framework. The covariance matrix includes the GNSS velocity uncertainties and the observation strength around the point to be interpolated. The ith diagonal term c_i is formulated as:

$$c_i = \sigma_i^2 S_i^{-1} = \sigma_i^2 (L_i Z_i)^{-1} \tag{6}$$

where σ_i^2 represents the variance of the ith velocity vector, L_i and Z_i denote the distance function and the spatial coverage function, respectively. The distance function is represented by the spatial smoothing parameter D_s and the distance to the ith observation ΔR_i:

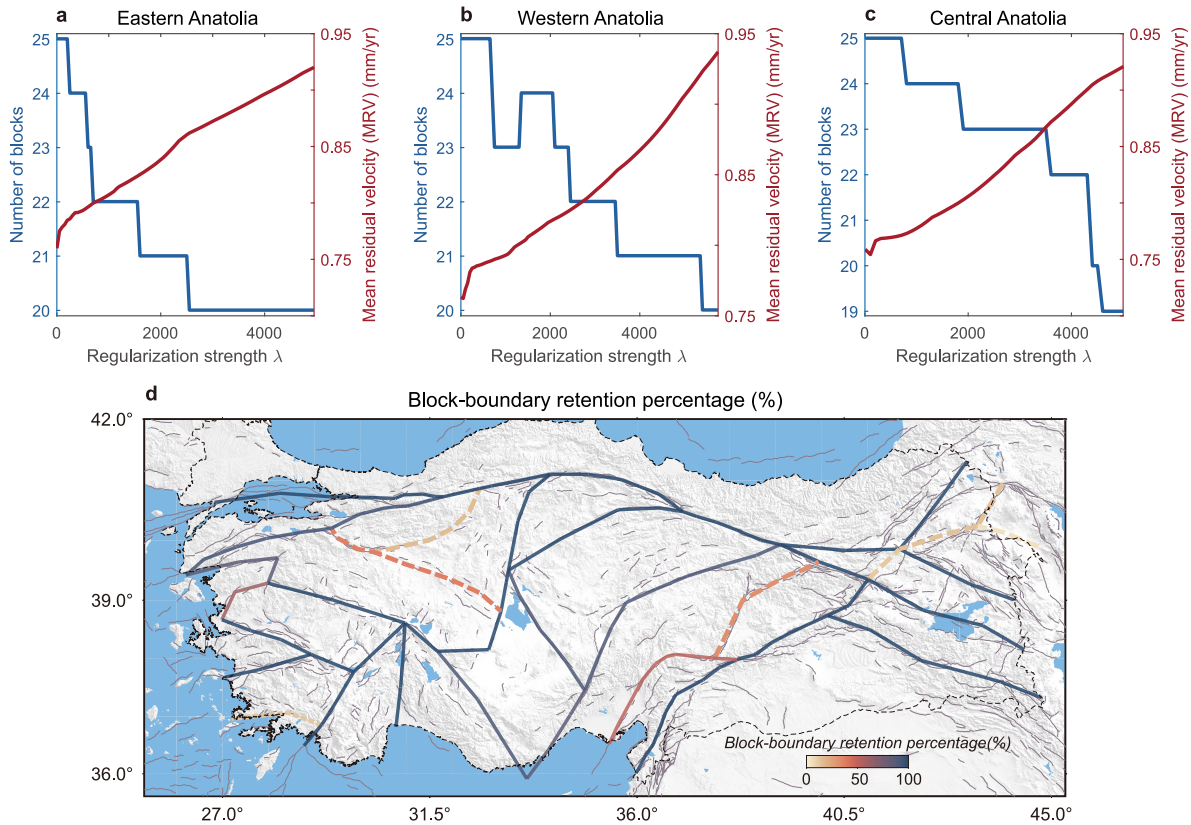

Figure 5. Variations in model fitting and block division with varying λ values. (a–c) Block numbers and Mean Residual Velocity (MRV) versus λ for eastern, western, and central Anatolia, respectively. (d) The boundary retention percentage across λ values. Dashed lines indicate boundaries discarded when MRV matches data uncertainty. All discarded boundaries had retention percentages below 50%.

$$L_i = \exp\left(-\frac{\Delta R_i^2}{D_s^2}\right) \tag{7}$$

D_s is adaptively adjusted by in situ data strength through the assignment of a threshold to $\sum_i S_i$, which is set to 18 following Zhao et al. (2022) due to comparable observation densities in both studies. The spatial coverage function is established through the Voronoi cells determined by the location of the observations:

$$Z_i = \frac{nS_i}{\sum_{k=1}^{n} S_k} \tag{8}$$

where S_i is the area of Voronoi cell for the ith observation. n is the number of cells.

Accordingly, the weight matrix constructed from this covariance matrix would assign greater weights to stations with shorter distances and larger spatial areas.

4. Results

4.1. Simplified Turkey Block Model Based on TVR Constraints

As shown in Figure 5, as the regularization strength increases, the number of blocks in Turkey progressively decreases while the Mean Residual Velocity (MRV) rises. To balance model complexity and misfit level, we selected the λ value where the MRV matches the systematic uncertainty of the observations (0.85 mm/yr; e.g.,

Huang & Evans, 2019). We also quantified the boundary retention percentage across all tested λ values, which clearly demonstrate how TVR controls boundary selection and the relative importance of different boundaries.

In eastern Turkey, we removed block boundaries within the Lesser Caucasus region where corresponding structures exhibited slip rates below 1 mm/yr in previous block models (Karakhanyan et al., 2013). We also removed the linkage between the KTJ and the Northeast Anatolian fault zone (NEAFZ), replacing it with a new boundary formed by the connection of the Tercan-Askale fault zone to the NEAFZ, a configuration not previously incorporated in block models to our knowledge. Additionally, the Malatya-Ovacık fault zone was removed, leaving the primary and secondary branches of the EAFZ to define the boundary between the Arabian and Anatolian plates. Dating results constrain the slip rate of the Malatya-Ovacık fault zone to only 1.0–1.1 mm/yr, indicating its limited role in local strain accumulation (Sançar et al., 2020).

In central Anatolia, we removed the boundaries along the Eskişehir fault zone and the Beypazarı blind thrust zone. The Eskişehir fault zone is generally recognized as an active dextral strike-slip system, with slip-rate reaching ∼5 mm/yr in the previous block model (Esat et al., 2021). The Beypazarı blind thrust zone exhibits a compressional rate of ∼3 mm/yr (Esat et al., 2021). However, in western Turkey, we identified three low-strain boundaries, two of which are again along the Eskişehir fault zone and the Beypazarı blind thrust zone. Thus, the activity of these faults requires further investigation.

The third proposed boundary for removal is the Gökova Graben, a well-documented active structure with significant seismicity (e.g., Yolsal-Çevikbilen et al., 2014). Its identification as inactive likely results from sparse geodetic coverage along its southern margin. We therefore retained this tectonically significant boundary despite potential uncertainties in the inferred slip rate. Consequently, our final model employs 19 tectonic blocks to interpret the surface velocity field across Turkey (Figure 5d).

4.2. Strain-Rate Field

The GNSS-derived strain-rate field for Turkey is depicted in Figure 6, with (a) displaying the second invariant of strain and the maximum shear strain rate, and (b) displaying the dilatation rate and the maximum/minimum principal strain rates. The maximum shear strain-rate field exhibits first-order consistency with the results of Weiss et al. (2020). Furthermore, the dense GNSS network constrains the N-S deformation gradient, enabling more robust estimates of uniform horizontal strain rates. In addition to capturing the E-W strike-slip motion along the NAFZ, this data set also resolves the spatial transition in strain fields from the near N-S strike-slip component at the Arabian-Anatolian plate boundary to the N-S extension in western Turkey.

High strain rates (exceeding 100 nstrain/yr) are observed along the NAFZ, indicating significant stress accumulation due to the relative motion between the Anatolian microplate and the Eurasian plate. The maximum strain rate reaches up to ∼250 nstrain/yr, with a significant proportion of shear strain (∼170 nstrain/yr) concentrated at the Izmit creep zone. Furthermore, notable high values of strain rates (30–90 nstrain/yr) are observed in western Anatolia, EAFZ, and East Anatolian Compression Province (Figure 6). These regional high-strain features are incorporated into corresponding major tectonic structures within our block model. Central Anatolia shows a low strain rate below ∼20 nstrain/yr, demarcated by block boundaries from the higher strain domains in eastern and western Turkey.

Additionally, we find that the directions of maximum shear strain rates in the strike-slip fault systems agree well with fault strikes, such as the nearly E-W dextral strike-slip along the NAFZ, the NE-SW sinistral strike-slip along the EAFZ, and NW-SE dextral and NE-SW sinistral strike-slip in the East Anatolian Compression Province (Figure 6a).

Our results clearly show that western Turkey and northeastern Turkey are dominated by extension and compression motions, respectively, with the maximum dilatation rate reaching ∼70 nstrain/yr and ∼−35 nstrain/yr. Obvious compression also exists in the West Taurides Thrust Fault (∼−16 nstrain/yr) and the EPCW (∼−20 nstrain/yr), which is consistent with the tectonic setting and geophysical findings (Elitez & Yaltırak, 2023; Esat et al., 2021). The EPCW also exhibits significantly higher shear strain rates compared to its surrounding areas, which justifies its retention as a block boundary in our model. Central Turkey exhibits widespread extension at a rate of ∼10 nstrain/yr (Figure 6b). In addition, the Büyük Menderes graben exhibits locally high tensile strain rate of ∼90 nstrain/yr and shear strain rate of ∼55 nstrain/yr. In general, the Turkey region exhibits

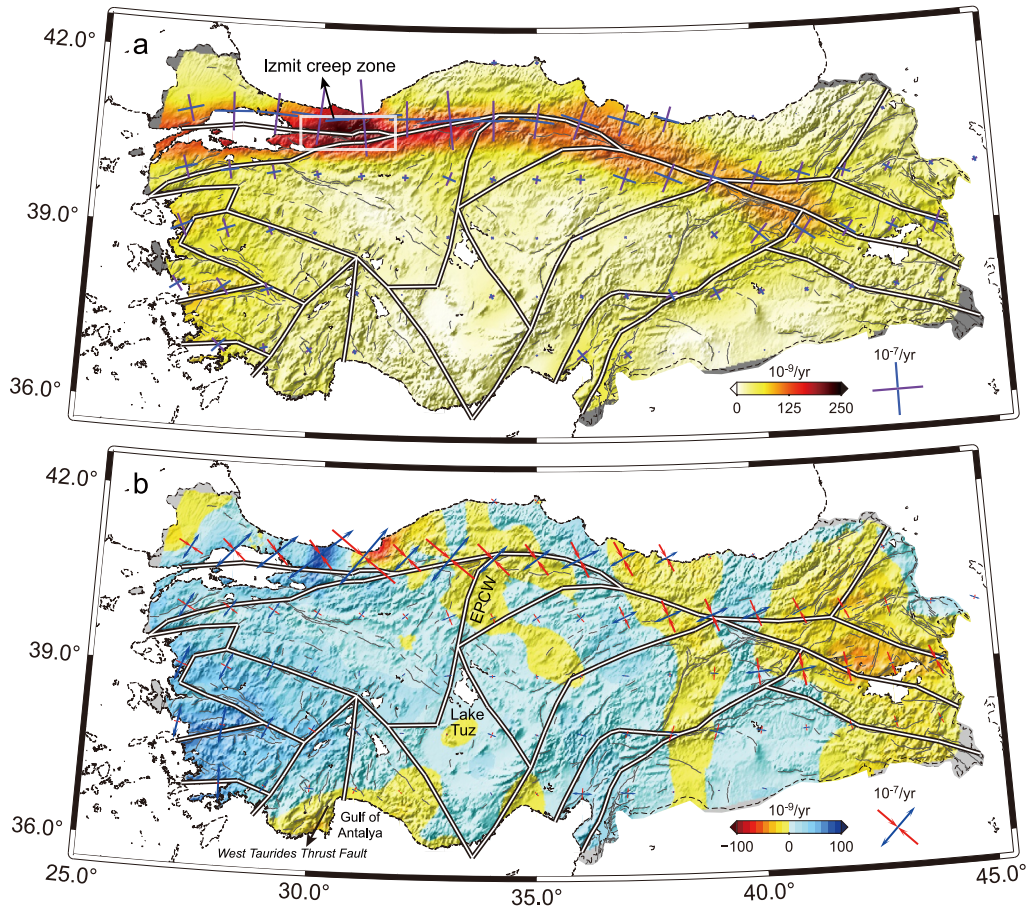

Figure 6. Global Navigation Satellite System strain-rate field for Turkey. Overlaying on the terrain are the second invariant (a) and the dilatation rate (b) of horizontal strain. The solid black lines represent the retained block boundaries. In this figure, the blue and purple bars in the crosses display the amplitudes and orientations of the dextral and sinistral maximum shear strain-rates, respectively. In this figure, the arrow pairs show the maximum and minimum principal strain rates, with the blue and red arrows indicating extension and contraction, respectively. Abbreviations: EPCW, Eldivan-Elmadağ pinched crustal wedge.

low internal strain surrounded by high peripheral strain, showing first-order consistency with the distribution of major earthquakes (Figure 2b).

4.3. Fault Slip Rates Derived From Block Modeling

The inverted strike-slip and tensile/dip-slip components of active fault motions are shown in Figure 7. The complex slip partitioning indicates spatially heterogeneous kinematics across Turkey under multi-plate interactions. The dextral strike-slip NAFZ, accommodating the majority of the relative motion between the Eurasian and Anatolian plates, exhibits a slip rate ranging from 16.4 ± 0.5 to 26.2 ± 0.2 mm/yr (Figure 7a). The fault zone bifurcates at both termini, with slip rates along the main branch exhibiting partial attenuation. To the west, the NAFZ splits into two branches in the Sea of Marmara, with most strain accumulated on the northern branch according to previous studies (Gasperini et al., 2011; Kurt et al., 2013). Our model indicates that the slip rates of the northern and southern branches are 22.2 ± 0.3 mm/yr and ~2–3 mm/yr, respectively. The estimated slip rate of the northern branch is consistent with the geodetic slip rate of ~25 mm/yr reported by Aktug et al. (2009), and comparable to the late-quaternary slip rate of ~18.5 mm/yr derived from seismic reflection data and geological models (Kurt et al., 2013). Moving eastward toward the KTJ, the slip rate of the NAFZ decreases to 16.4 ± 0.5 mm/yr. This supports the eastward decreasing model proposed by Aktug, Dikmen, et al. (2013), but is higher than their estimated rate of ~12 mm/yr. In contrast, our result shows better agreement with the

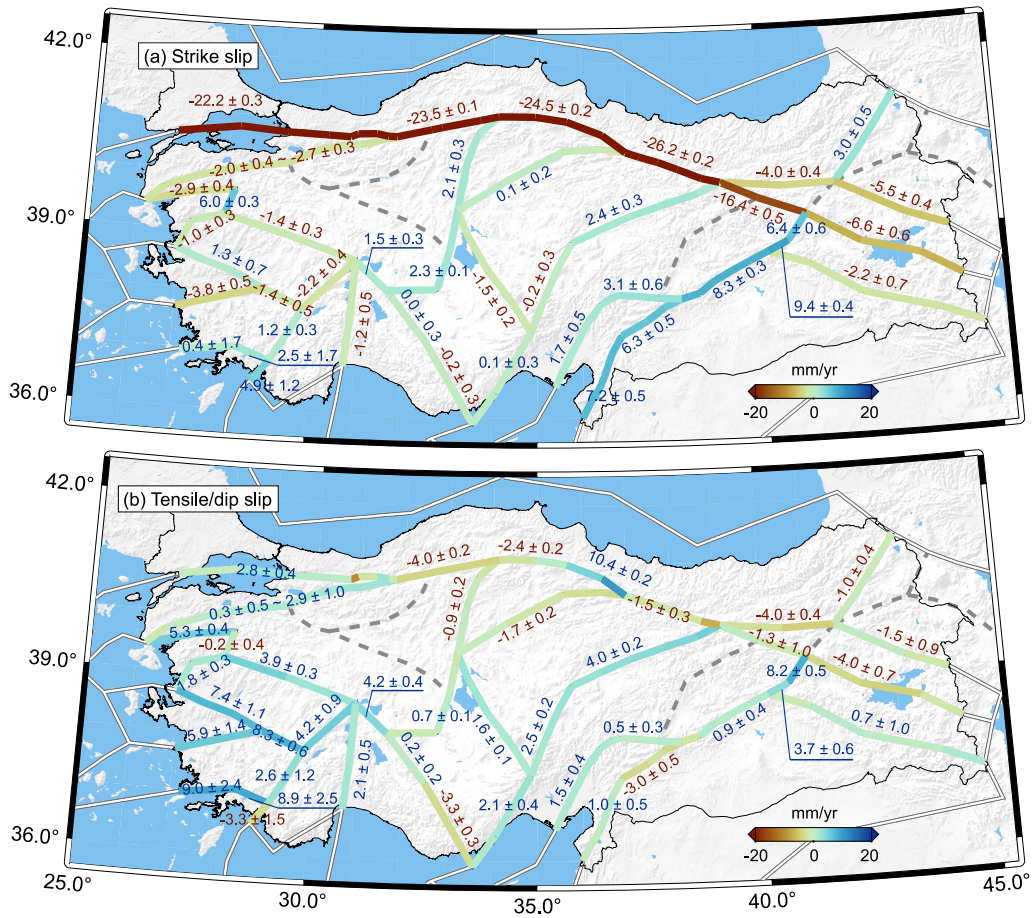

Figure 7. Strike-slip and tensile/dip-slip rates of active faults in Turkey. Positive slip rates indicate (a) sinistral strike-slip and (b) extensional motions. White lines depict the block boundaries defined outside Turkey. Dashed lines denote boundaries discarded by the total variation regularization algorithm.

geomorphic estimates of 18 ± 3.5 mm/yr (Hubert-Ferrari et al., 2002). The decaying slip rate appears to be accommodated by the Tercan-Askale fault zone, which shows a dextral slip rate of 4.0 ± 0.4 mm/yr. East of the KTJ, the North Anatolian Continuum fault zone shows a dextral slip rate of 6.6 ± 0.6 mm/yr and a contraction rate of 4.0 ± 0.7 mm/yr, indicating N-S tectonic compression under continental collision. Similar kinematics are observed along the Çaldıran fault, with a dextral strike-slip rate of 5.5 ± 0.4 mm/yr and a compression rate of 1.5 ± 0.9 mm/yr (Figure 7).

The EAFZ is another major strike-slip fault system in Turkey. Previous geodetic and geological studies suggested that the EAFZ maintains a constant sinistral strike-slip rate of ~10 mm/yr north of Türkoglu, which then notably decreases to ~4 mm/yr in the southwest (Aktug et al., 2016; Reilinger et al., 2006; Yönlü et al., 2017; Özkan et al., 2023). For instance, based on field investigations and geodetic data, Yönlü et al. (2017) proposed that the fault slip east of Türkoglu (10 mm/yr) is transferred to the Cyprus arc (2–3 mm/yr) and the Dead Sea fault zone (4.5 mm/yr), respectively. Our study confirms a significant shear partitioning at the junction of the EAFZ and the Sürgü fault. The slip rate along the EAFZ decreases from 8.3 ± 0.3 to 6.3 ± 0.5 mm/yr, concurrently, the Sürgü-Çardak fault accommodates sinistral slip-rate of 3.1 ± 0.6 mm/yr. The determined slip rate for the Sürgü-Çardak fault is consistent with geomorphic investigations (Duman & Emre, 2013) and the Seismic Source Characterization Model (Gülerce et al., 2017). These results suggest that secondary branch of the EAFZ absorbs a considerable portion of the relative motion between the Arabian and Anatolian plates, shedding light on the seismogenic mechanism of the 2023 Mw 7.8 and Mw 7.5 earthquake doublet (He et al., 2023; Jia et al., 2023). We also determine a sinistral slip rate of 2.4 ± 0.3 mm/yr along the northern CAFZ, which rapidly decays to

negligible levels along the Ecemiş fault. Field investigations reveal a slip rate of ∼1 mm/yr for the Ecemiş fault, a value challenging to robustly detect with GNSS-constrained block models (Yıldırım et al., 2016). Besides, significant extension is observed along the CAFZ, decreasing from 4.0 ± 0.2 mm/yr in the northern segment to 2.5 ± 0.2 mm/yr in the southern segment.

To the northwest of the Eastern Anatolian shear zone lies the Central Anatolian province (Esat et al., 2021; Gezgin et al., 2022; Seyitoglu et al., 2022a). Geological observations and focal mechanism solutions from previous studies indicate that the Tuzgölü and Eskişehir fault zones are predominantly dextral strike-slip motion with relatively low seismicity (Seyitoglu et al., 2015). Our results indicate a right-lateral slip rate of 1.5 ± 0.2 mm/yr for the Tuzgölü fault zone, whereas the Eskişehir fault zone was excluded during block model construction. We also determined a left-lateral slip rate of 2.1 ± 0.3 mm/yr and a contraction rate of 0.9 ± 0.2 mm/yr for the EPCW. Esat et al. (2021) developed a detailed block model in this domain and determined higher dextral slip rates of ∼5 mm/yr for the Tuzgölü fault zone and ∼6 mm/yr for the Eskişehir fault zone, along with a contraction rate of 12.5 ± 3.2 mm/yr for the EPCW. The slip rates reported by Esat et al. (2021) seem generally overestimated, such as the maximum strike-slip rate of the EPCW reaching 11.7 mm/yr, which is inconsistent with the historically low seismic activity and regional InSAR observations (Weiss et al., 2020).

The graben system in western Anatolia is one of the most seismically active areas in the world, characterized by widespread and rapid extension (Dewey & Şengör, 1979). Our results show that the regional extensional rate increases rapidly from ∼20 mm/yr at 29° latitude to ∼30 mm/yr at 27° latitude, falling within the range of 20 mm/yr to 30 mm/yr documented by previous geodetic studies (Aktug et al., 2009; McClusky et al., 2000; Reilinger et al., 2006). The FBFZ is dominated by extension, with rates decreasing from 4.2 ± 0.9 mm/yr in the northern segment to 2.6 ± 1.2 mm/yr in the southern segment. Concurrently, the northern segment exhibits 2.2 ± 0.4 mm/yr of dextral strike-slip motion, while the southern segment shows 1.2 ± 0.3 mm/yr of sinistral strike-slip component. This strike-slip transition pattern is consistent with previous block model results, though the magnitude of southern segment motion is significantly lower than prior estimates of 5–8 mm/yr (Aktug et al., 2009; Elitez et al., 2016; Tiryakioğlu et al., 2013).

4.4. Residual Analysis of Block Model Inversion

Beyond reliable slip rate estimates, our results also include some anomalous values. For instance, at the northern termination of the EAFZ near its junction with the NAFZ, extension rates reach 8.2 ± 0.5 mm/yr. Further analysis of residual spatial patterns may help elucidate these phenomena.

The spatial distribution and statistical analysis of model residuals are shown in Figure 8. The residuals display a spatially random pattern (Figure 8a). Histogram analysis for the E-W and N-S components of the residuals indicates that both components approximate a normal distribution, with means and standard deviations of −0.11/0.83 mm/yr for E-W residuals and 0.08/0.91 mm/yr for N-S residuals, respectively (Figure 8b). All blocks exhibit the mean absolute residuals smaller than data uncertainties, except for the Sea of Marmara block (Figure 8c). These suggest an overall good fit to the observations.

Meanwhile, approximately 10% of the residuals exceed the 95% confidence interval, with the maximum residual (∼4.5 mm/yr) localized near the KTJ. East of this large residual, the extensional rate along the EAFZ reaches 8.3 ± 0.5 mm/yr. This motion would theoretically drive the stations westward, directly opposing the observed residual direction. This implies that the heterogeneous deformation surrounding the KTJ challenges conventional block-model assumptions, reflecting instead the intricate kinematics of local fault networks (Figure 1a).

Additionally, significant residuals are observed west of the EPCW, bounded by the Abdüsselam pinched crustal wedge, which was excluded from our block model (Figure 3). These large residuals appear to reflect local deformation across discontinuous structures. Besides, some significant intra-block residuals persist in western and southeastern Turkey, possibly related to non-tectonic processes (e.g., hydrology). These residuals remain acceptable as they show no systematic spatial pattern compared to the well-fit data.

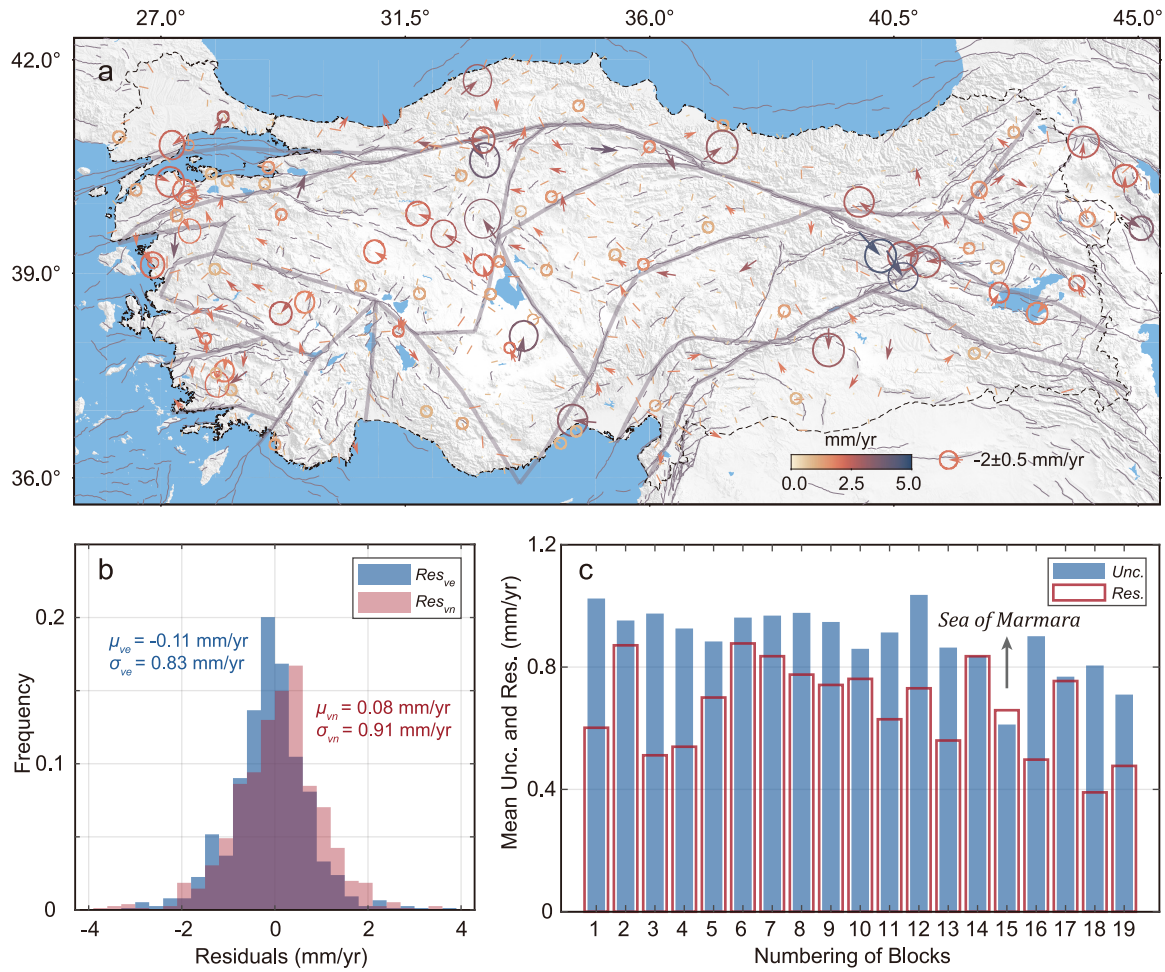

Figure 8. Residual velocity distribution and statistics of the block model. (a) Spatial distribution of residual velocities, colored by amplitude. Residual vectors with confidence ellipses indicate values exceeding the 95% confidence interval. (b) Histogram statistics of E-W and N-S residuals. μ_{ve} and σ_{ve} represent the mean and standard deviation of the E-W residuals, respectively. μ_{vn} and σ_{vn} represent the corresponding statistics of the N-S residuals. (c) Histogram comparison of mean absolute residuals (red) versus mean uncertainties (blue) for each block.

5. Discussion

5.1. Performance Analysis on the Constructed Block Model: Improvements and Limitations

Previous studies on block models for Turkey can be roughly categorized into two types: those focusing on local tectonics (e.g., Aktug et al., 2009; Aktug et al., 2013a; Esat et al., 2021) and those addressing plate- or microplate-scale dynamics (e.g., Ergintav et al., 2023; Reilinger et al., 2006; Seyitoglu et al., 2022a). Our TVR-optimized model bridges this gap by simultaneously resolving both primary and secondary fault kinematics under a unified dynamic framework.

Conventional block models simplify the EAFZ as a single boundary, typically estimating slip rates of 9–10 mm/yr along the northeastern segment (Figure S5 in Supporting Information S1; Aktug et al., 2016; Özkan et al., 2023; Reilinger et al., 2006). While Özbey et al. (2024) recently proposed an alternative configuration incorporating the Malatya-Çardak fault, this geometry appears inconsistent with the known structural divergence of the main and secondary EAFZ branches at Çelikhan as documented by Duman & Emre (2013). Our analysis using the TVR optimization approach evaluated the Malatya, Sürgü and Çardak faults as potential block boundaries, ultimately identifying the Malatya fault as inactive while confirming activity along the secondary EAFZ branch. The results demonstrate clear slip partitioning along the EAFZ, with slip-rates of 8.3 ± 0.3 mm/yr for the northeastern

segment transitioning to 3.1 ± 0.6 mm/yr on the secondary branch and 6.3 ± 0.5 mm/yr on the southwestern segment.

Existing block models of the KTJ region consistently delineate three blocks bounded by the NAFZ, EAFZ, and NEAFZ (Figure S6 in Supporting Information S1; Aktug, Dikmen, et al., 2013; Reilinger et al., 2006; Walters et al., 2014). Our initial four-block configuration introduced a new NAFZ-NEAFZ connection through the Tercan fault. The TVR inversion preserved the proposed Tercan fault boundary and discarded the KTJ-NEAFZ connection. This result agrees well with geological evidence identifying the Tercan fault's northeastward extension as the boundary of the East Anatolian Compressional Province (Figure 1b), further supported by concentrated seismicity along its trace compared to minimal activity between KTJ and NEAFZ (Figure 2b). East of the KTJ, N-S compression and E-W shear under the Arabian-Eurasian convergence are modeled onto the BZSZ and the Çaldıran fault in previous models (e.g., Djamour et al., 2011; Reilinger et al., 2006). The derived geodetic strike-slip rate of ∼8–12 mm/yr for the Çaldıran fault is significantly higher than the geological slip rate of ∼3.27 mm/yr obtained from the offset of lithological contacts (Selçuk et al., 2016). Our TVR-optimized model reconciles this discrepancy by estimating 5.5 ± 0.4 mm/yr along the Çaldıran fault while simultaneously retaining the seismically active North Anatolian Continuum fault as a block boundary, delivering a geologically consistent solution that reduces seismic hazard uncertainties.

These findings demonstrate how oversimplified block models may underestimate seismic hazards from secondary faults (e.g., 2023 Mw 7.5 Elbistan earthquake) while exaggerating boundary fault hazards (Selçuk et al., 2016). However, increased model complexity does not necessarily improve accuracy, as exemplified by the nine-block model of north Central Anatolia in Esat et al. (2021) (Figure S7 in Supporting Information S1). Their solution determines >10 mm/yr compressional rate along the EPCW, accompanied by uniform extensional residuals on both sides, indicating rate overestimation. Our simplified model excludes inactive Eskişehir fault and Beypazari blind thrust zone, obtaining more plausible EPCW motion of 0.9 ± 0.2 mm/yr contraction with 2.1 ± 0.3 mm/yr left-lateral slip.

Early studies suggested that the kinematics in western Turkey could be explained by a few rigid blocks, with intra-block strain rates (∼30–50 nstrain/yr) being 1–2 orders of magnitude lower than those across microplate boundaries (∼500–1,000 nstrain/yr) (Nyst & Thatcher, 2004; Reilinger et al., 2006). As the number of GNSS observations increased, microplate-scale inversions showed obvious residuals near some active faults (Aktug et al., 2009; Ergintav et al., 2023). Aktug et al. (2009) concluded that a block model with a scale smaller than ∼50 km or a continuum model with a distributed strain rate of 50 nstrain/yr can properly interpret the GNSS velocity field. This interpretation is further supported by high-spatial-resolution InSAR observations (Diercks et al., 2024). Our block model builds on Aktug et al. (2009), with the TVR algorithm preserving all original boundaries. Nevertheless, significant inversion residuals persist, indicating that internal strain cannot be neglected, particularly for regional seismic hazard assessments.

5.2. Regional Seismic Activities and Tectonic Implications

The large-scope and dense GNSS observations in Turkey offer a unique opportunity to systematically analyze the intricate tectonic structures and deformation patterns on a national scale. By integrating focal mechanisms, active fault motions, and continuous strain rates, we further analyze the deformation mechanisms and kinematics of the main active structures across Turkey (Figure 9).

The collision and convergence between the Arabian and Eurasian plates have induced large-scale deformation in northeastern Turkey, forming a series of conjugate structures across the Turkish-Iranian Plateau (Figure 1). The coexistence of strike-slip and thrust mechanisms in this region indicates that, in addition to the dominant N-S compression, NW-SE-oriented faults also accommodate a significant portion of the convergence through strike-slip motion, as evidenced by the maximum shear strain field. Similar large-scale deformation patterns are observed in western Turkey, manifested by widespread normal-faulting earthquakes, extensional strain fields, and active graben development. The prevalence of strike-slip mechanisms along the NAFZ-EAFZ system reveals their essential role in accommodating Anatolian lateral movement. Orientations of the maximum shear of secondary structures in eastern Anatolia show a good agreement with those along the EAFZ, demonstrating a common shared driving force (Figure 6a). Moreover, our block modeling results suggest that the structures, including the CAFZ and Çardak-Savrun fault, are dominated by sinistral strike-slip movement (Figure 7a). This implies that the extensive deformation within Anatolian microplate from the Arabia-Eurasia convergence extends

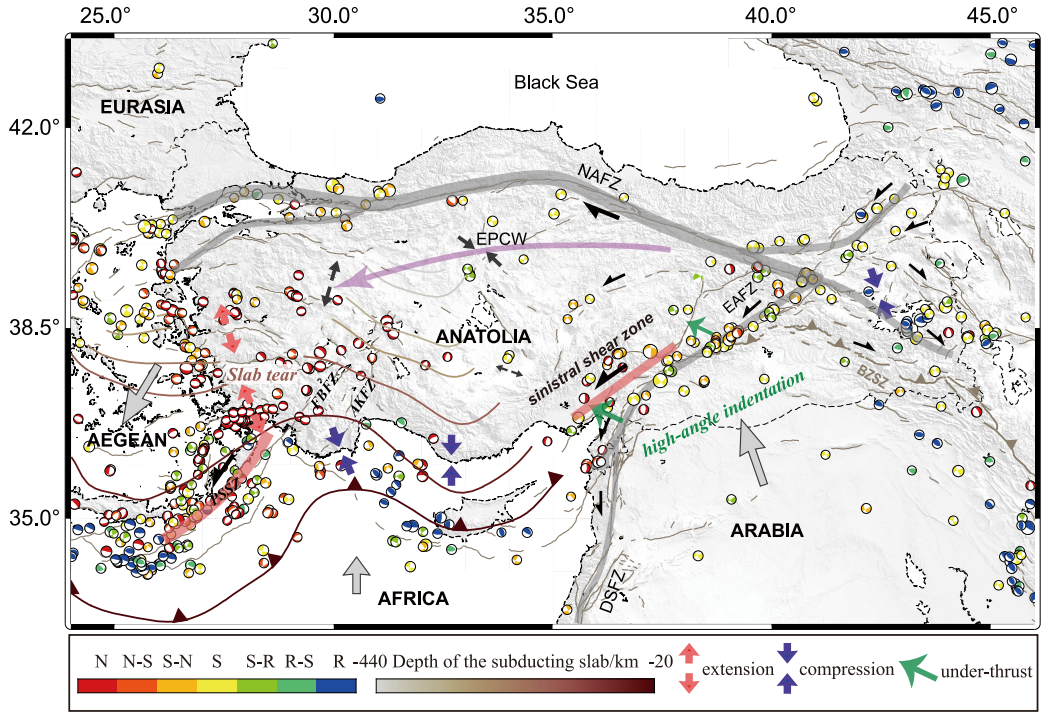

Figure 9. Schematic diagram of active tectonic structures in Turkey and surrounding regions. The focal mechanism solutions are from Global Centroid Moment Tensor (https://www.globalcmt.org), over the period from January 1976 to December 2023, with magnitude greater than Mw 5.0. The depth contour data for the subducting slab is obtained from the Slab2 model (Hayes et al., 2018). The thick gray lines show strike-slip fault zones forming a large conjugate strike-slip system across Turkey. The thick pink lines mark sinistral shear zones in eastern Anatolia and along the PSSZ. Gray arrows denote plate motion directions. The purple arrow indicates the intraplate stress rotation zone. Red and blue arrow pairs represent extensional and compressional strains, respectively. The green arrow indicates the high-angle indentation by Arabia into the Anatolian microplate. Abbreviations: N, normal; S, strike-slip; R, reverse; FBFZ, Fethiye-Burdur Fault Zone; PSSZ, Pliny-Strabo Shear Zone; AKFZ, Antalya-Kekova Fault Zone; EPCW, Eldivan-Elmadağ Pinched Crustal Wedge; NAFZ, North Anatolian Fault Zone; EAFZ, East Anatolian Fault Zone; and DSFZ, Dead Sea Fault Zone.

as far west as the CAFZ. Furthermore, we find that the slip rate of the entire sinistral system decreases from ~12 mm/yr in the northeast to ~9 mm/yr in the southwest. However, further west to the Ecemiş-Deliler fault zone, no notable strike-slip component can be detected (Figure 7a). This finding contradicts the view of Seyitoglu et al. (2022b) that a tectonic escape channel is formed between the strike-slip system in eastern Anatolia and the Antalya-Kekova fault zone and Pliny-Strabo fault zone to its west through two restraining stepovers (Figure 9).

An alternative yet debatable view is that the Pliny-Strabo fault zone structurally links with the FBFZ, constituting a coupled escape structure (Elitez et al., 2016; Elitez & Yaltırak, 2016, 2023). The Pliny-Strabo fault zone has been well-determined as a sinistral shear zone resulting from slab tearing in previous studies (Figure 9; Berk Biryol et al., 2011; Özbakır et al., 2013). The controversy regarding the FBFZ arises from discrepancies between geodetically observed sinistral strike-slip motion (typically defined via block modeling or velocity difference analysis) and normal faulting mechanisms in the earthquake catalog. The limitations of block modeling in western Turkey have been discussed in the preceding chapter. While the velocity difference approach adopted by Elitez et al. (2016) notably neglected rotational components in the velocity vectors, which is particularly significant in western Turkey, resulting in an overestimation to 8–10 mm/yr. The supporting tectonic interpretation is that the FBFZ acts as a strike-slip transition area to accommodate the Hellenic retreat in the west and Taurides thrusting in the east (Elitez & Yaltırak, 2023). We further investigate local tectonic interactions based on the regional principal strain-rate field (Figure S8 in Supporting Information S1). The strain-rate field clearly shows that the Taurides thrusting only affects the local strain rotation, while the FBFZ is primarily controlled by uniaxial extension and lacks tectonic stresses that form strike-slip motion (Figure S8 in Supporting Information S1). These findings are consistent with the implications from focal mechanism investigations of recent earthquakes in Nissen

et al. (2022), demonstrating the absence of strike-slip continuity between the FBFZ and Pliny-Strabo fault zone to form an escape pathway.

The westward escape of the Anatolian microplate is also accompanied by intra-plate stress rotation, with the tectonic transform in north Central Anatolia being particularly noticeable (Figures 6 and 7). As shown in Figures 6 and 7, this tectonic domain is characterized by sinistral shear accompanied by extension along the CAFZ, compression in the EPCW, and extension combined with dextral strike-slip along the Simav fault zone, progressing from east to west. The regional principal strain rates show counterclockwise rotation along the trajectory of the purple solid line in Figure 9. This indicates that the wide-spread deformation within Anatolia microplate from the Eurasian-Arabian convergence terminated near the CAFZ, while the EPCW and Simav fault zone, which continue to cross westward, are mainly influenced by the lateral interaction between Eurasia and Anatolia and the rollback of the Aegean slab. Esat et al. (2021) suggested that the contraction in the EPCW may result from a complex interaction between nearly N-S contraction in eastern Anatolia and N-S extension in western Anatolia. However, we find that the principal strain-rate components around the EPCW are significantly greater than the strain-rate values on its eastern and western sides, indicating that regional compression is not only an adjustment to stress differences between the two sides. Furthermore, we observe that the EPCW is located ∼125 km southwest of the maximum bend (∼37°) of the NAFZ. Barbot & Weiss (2021) proposed that the high kinematic compatibility between the bend and the overall rotation of Anatolia results in the absence of conjugate structures or topographic variations. This view contradicts the angular discrepancy between the velocity vectors and the strike of the NAFZ and ignores the temporal heterogeneity of strain during the evolution of the NAFZ. Here, the compression observed along the EPCW matches the strain concentration expected to be formed by a restraining bend (Cunningham & Mann, 2007). Moreover, we find that the distance between EPCW and maximum bending (∼125 km) is close to the distance between Erzincan and the KTJ (∼130 km). The passage between Erzincan and KTJ is a manifestation of the migration from the EAFZ and its predecessors (Bozkurt, 2001). This implies that the contraction in the EPCW could be the tectonic response to the bend during the formation and westward movement of the escape system, like the conjugate structures at Erzincan and the KTJ and the western and eastern Transverse Ranges at the big bend of the San Andreas Fault (Barbot & Weiss, 2021; Daout et al., 2016). Concurrently, the rapid extrusion of Anatolia drove the progressive development of parallel thrust belts in northern Central Anatolia, while simultaneously inhibiting the stable localization of strain necessary to generate obvious topography. In contrast, southward away from the NAFZ, the fault system consistently exhibits extensional deformation. For instance, the Tuzgölü fault zone accommodates ∼1.6 mm/yr of extension, which likely accounts for the formation of Lake Tuz within its hanging wall.

5.3. On-Fault and Off-Fault Moment Accumulation Rates Across Turkey

To systematically assess seismic hazard across Turkey, we estimate moment accumulation rates both on and off faults by integrating block-modeled slip rates with continuous strain-rates. Based on the geometry of major block boundaries, we tessellate the Turkey region into multiple triangular patches with a ∼40 km sampling interval along faults. We can therefore quantify moment accumulation rates for individual fault segments and block patches. Specifically, the on-fault moment rate can be estimated using $\dot{M}_{\mathrm{on}} = \mu w l S$, where μ is the shear modulus of the rocks (set to 3.2×10^{10} N/m^2 following Simão et al. (2016)). w and l represent the fault width and length, respectively. S denotes the fault slip rate (e.g., Bird & Liu, 2007). The off-fault moment rate can be estimated using $\dot{M}_{\mathrm{off}} = 2\mu H_s A[\mathrm{Max}(|\varepsilon_{H\mathrm{max}}|, |\varepsilon_{H\mathrm{min}}|, |\varepsilon_{H\mathrm{max}} + \varepsilon_{H\mathrm{min}}|)]$, where $\varepsilon_{H\mathrm{max}}$ and $\varepsilon_{H\mathrm{min}}$ represent the maximum and minimum principal strain rates extracted from the strain tensor, respectively (Savage & Simpson, 1997). We assign a strain tensor to each tectonic block by calculating the mean internal strain within regions far away from major faults. H_s is the thickness of the seismogenic layer. A denotes the area of each patch. The relevant fault parameters are consistent with those defined in the block model.

The estimated on- and off-fault moment rates are shown in Figure 10. We further overlay the block inversion residuals to account for potential deformation signals that might otherwise be overlooked. Our results show that the segments with moment rates exceeding 1.5×10^{17} Nm/yr are mostly located along the NAFZ and its eastern continuation, correlating well with high seismicity along this fault system. Moderately high moment rates ($>10^{17}$ Nm/yr) occur along the Çaldıran fault, Tercan fault, southeastern segment of the EAFZ, and normal fault systems in western Turkey. These faults also exhibit high seismic activity, though less intense than the NAFZ. Other faults with low moment rates exhibit minimal seismic activity, such as secondary faults within the central

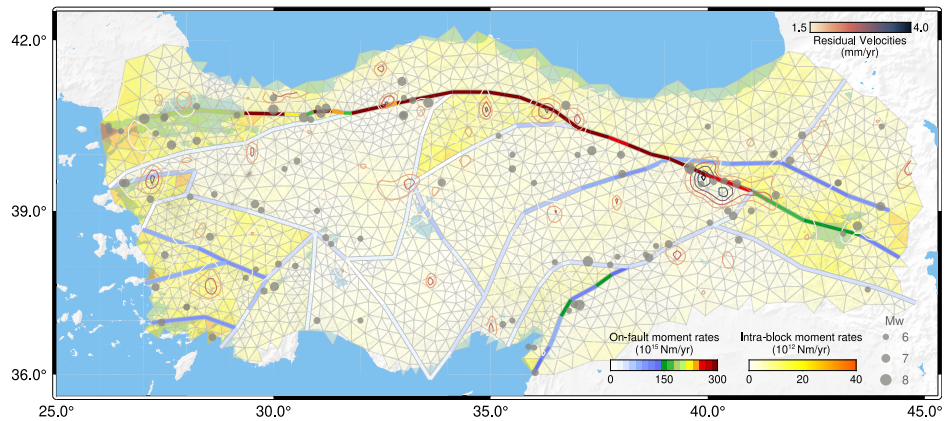

Figure 10. Moment accumulation rate distribution across Turkey. On-fault moment rates are estimated from block-modeled slip rates, while intra-block rates are derived from continuous strain rate field. The earthquake catalog spans 1900–2025 with Mw ≥ 5.9. Contours indicate the magnitude of block inversion residuals.

Turkey. Significant off-fault deformation is observed in northeastern Turkey, western Turkey, and near the restraining bend of the NAFZ in central Turkey, where obvious block inversion residuals are also found (Figure 10). Other regions in central and eastern Turkey exhibit limited off-fault deformation, with correspondingly minor block inversion residuals. Notable internal block deformation in western Turkey is consistent with sporadic seismic activity. Pronounced seismicity exists between the CAFZ and the Kirikkale-Erbaa fault zone. The linear alignment of these earthquakes reveals the structural complexity of this block interior, as evidenced by its parallel fault systems (Figure 1). Nevertheless, GNSS-constrained block model shows good fit, with homogeneous and low-magnitude internal strain (Figures 6 and 8). Further seismic hazard assessment integrating focal mechanisms and field investigations is essential for this region.

The total on-fault and off-fault moment rates are 2.44×10^{19} Nm/yr and 1.82×10^{16} Nm/yr, respectively, differing by three orders of magnitude. Based on the moment-magnitude relationship (Hanks & Kanamori, 1979), the annual on-fault energy accumulation is equivalent to an Mw 6.9 earthquake, whereas the off-fault energy corresponds to an Mw 4.8 event.

The comparison between earthquake released moment and geodetic-inferred moment accumulation serves to validate the effectiveness of our moment-rate model for regional seismic hazard assessment. Using the compiled earthquake catalog, we calculate a cumulative seismic moment release of 2.95×10^{21} Nm since 1900 (Figure 11). Given the dominant contribution of large earthquakes to energy release estimates, we also calculate the total moment by adopting USGS-reported magnitudes for earthquakes with Mw ≥ 7.5, obtaining 3.48×10^{21} Nm. Over the same period, the on-fault and off-fault geodetic moment accumulation totals 3.05×10^{21} Nm, which is consistent with the seismic release magnitude (Figure 11).

The temporal evolution of cumulative seismic moment release exhibits a characteristic step-like pattern, with each step corresponding to the occurrence of a major earthquake (Figure 11). This release process maintains a 0.96 correlation with the geodetically-derived moment accumulation. Our analysis reveals a period of ~30 years from 1945 to 1976 showing steady energy release at a rate consistent with the geodetically derived moment accumulation rate. Notably, periods lasting about 20 years with significantly reduced moment release preceded the 1939–1944 earthquake sequence, the 1999 Mw 7.6 event, and the 2023 earthquake doublet, with release rates markedly lower than the stable rate from 1945 to 1976. These findings suggest that tectonic quiescence may indicate elevated major earthquake potential, while stable moderate-magnitude energy release corresponds to lower risk. Our analysis underscores the critical need to incorporate a systematic moment deficit perspective into seismic hazard evaluation frameworks. Moving forward, we propose developing next-generation probabilistic seismic hazard models for Turkey by integrating earthquake catalogs, geodetic observations, and regional fault kinematics to enhance predictive capability (e.g., Bird et al., 2010, 2015; Shen & Bird, 2022).

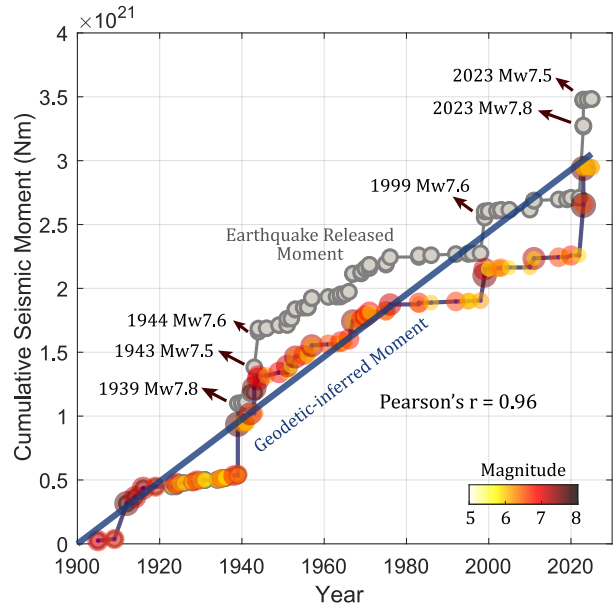

Figure 11. Comparison between earthquake released moment and geodetic-inferred accumulated moment. Colored dotted line shows cumulative moment release (Mw ≥ 5.9) from 1900 to 2025 using the compiled earthquake catalog. Gray dotted line represents cumulative release adopting USGS-reported magnitudes for earthquakes with Mw ≥ 7.5. Solid line shows geodetic-inferred moment (Pearson correlation coefficient = 0.96 with the colored dotted line).

6. Conclusions

In this study, we investigated present-day kinematics and seismic hazards in Turkey using dense GNSS observations. By incorporating multi-source data sets and TVR optimization, we constructed an elastic block model comprising 19 blocks to characterize the tectonic deformation across Turkey. Our analysis revealed that the data-driven TVR block modeling demonstrates robust performance, effectively incorporating essential secondary faults while maintaining model simplicity. We identified contrasting deformation patterns at plate boundaries, characterized by localized strain accumulation along the NAFZ and partitioned slip transfer within fault systems across northeastern Turkey and the EAFZ. The compression in the EPCW and its adjacent parallel thrust belts appears linked to large bending of the NAFZ during long-term and rapid Anatolian extrusion. We found negligible left-lateral strike-slip motion along the Ecemiş-Deliler fault zone, indicating its failure to integrate with the AKFZ into a coherent tectonic escape system, while the FBFZ lacks the tectonic stress regime required to form an onshore strike-slip connection with the PSFZ. Furthermore, the geodetically inferred cumulative moment accumulation since 1900 broadly balances the released seismic moment. When the seismic moment release rate remains persistently lower than the accumulation rate for an extended period, it may suggest heightened potential for major earthquakes. These findings collectively provide an improved kinematic framework that enhances our understanding of Anatolian fault-system behavior and enables improved seismic hazard assessment by characterizing strain accumulation and release patterns for Turkey. Our study highlights the necessity of integrating geodetic observations with long-term seismic catalogs to develop advanced probabilistic seismic hazard models for Turkey.

Conflict of Interest

The authors declare no conflicts of interest relevant to this study.

Availability Statement

Modern earthquake catalogs used in this study can be downloaded from https://sites.google.com/site/xonurtan/turhec and https://deprem.afad.gov.tr/event-catalog. The online version of the active fault database used in this

study can be accessed at http://neotec.ginras.ru/index/mapbox/database_map.html. The code for the strain-rate calculation is available at http://scec.ess.ucla.edu/~zshen/visr/. The integrated GNSS velocity field, compiled earthquake catalog, and software used for block modeling can be downloaded from Zenodo (Sun, 2025).

Acknowledgments
We thank the editor Anke Friedrich, the associate editor Anne Socquet, Romain Jolivet, and an anonymous reviewer for thorough, thoughtful reviews that significantly improved the manuscript. We thank Onur Tan for sharing the compiled Historical Earthquake Catalogue of Turkey and the updated TURHEC. We also warmly thank Gürol Seyitoğlu and Korhan Esat for sharing the block boundary files. We are grateful to Eileen Evans for her guidance on the Total Variation Regularization algorithm. This work was supported by National Natural Science Foundation of China (42388102, 42304037, 41874024), Natural Science Foundation of Hunan Province (2024JJ3031), Special Fund of Institute of Earthquake Forecasting, China Earthquake Administration (CEAIEF20240404), Science and Technology Innovation Program of Fujian Province (2021Y3001), Science and Technology Innovation Program of Hunan Province (2023SK2012), and Fundamental Research Funds for the Central Universities of Central South University (2024ZZTS0368). Most of figures were produced by Generic Mapping Tools 6.4.0 software (Wessel et al., 2019).

References

Akin, U. (2016). Investigation of the seismic velocity distribution and crustal structure of Turkey by means of gravity data. *Bulletin of the Mineral Research and Exploration*, *153*, 185–202. https://doi.org/10.19111/bmre.01024

Aktug, B., Dikmen, U., Dogru, A., & Ozener, H. (2013). Seismicity and strain accumulation around Karliova Triple Junction (Turkey). *Journal of Geodynamics*, *67*, 21–29. https://doi.org/10.1016/j.jog.2012.04.008

Aktug, B., Nocquet, J. M., Cingöz, A., Parsons, B., Erkan, Y., England, P., et al. (2009). Deformation of western Turkey from a combination of permanent and campaign GPS data: Limits to block-like behavior. *Journal of Geophysical Research*, *114*(B10), 2008JB006000. https://doi.org/10.1029/2008JB006000

Aktug, B., Ozener, H., Dogru, A., Sabuncu, A., Turgut, B., Halicioglu, K., et al. (2016). Slip rates and seismic potential on the East Anatolian fault system using an improved GPS velocity field. *Journal of Geodynamics*, *94–95*, 1–12. https://doi.org/10.1016/j.jog.2016.01.001

Aktug, B., Parmaksız, E., Kurt, M., Lenk, O., Kılıçoğlu, A., Gürdal, M. A., & Özdemir, S. (2013a). Deformation of Central Anatolia: GPS implications. *Journal of Geodynamics*, *67*, 78–96. https://doi.org/10.1016/j.jog.2012.05.008

Armijo, R., Meyer, B., Hubert, A., & Barka, A. (1999). Westward propagation of the North Anatolian fault into the northern Aegean: Timing and kinematics. *Geology*, *27*(3), 267–270. https://doi.org/10.1130/0091-7613(1999)027<0267:WPOTNA>2.3.CO;2

Barbot, S., & Weiss, J. R. (2021). Connecting subduction, extension and shear localization across the Aegean Sea and Anatolia. *Geophysical Journal International*, *226*(1), 422–445. https://doi.org/10.1093/gji/ggab078

Basili, R., Kastelic, V., Demircioglu Tumsa, M. B., Garcia Moreno, D., Nemser, E. S., Petricca, P., et al. (2013). The European database of seismogenic faults (EDSF) compiled in the framework of the project SHARE. https://doi.org/10.6092/INGV.IT-SHARE-EDSF

Berk Biryol, C., Beck, S. L., Zandt, G., & Özacar, A. A. (2011). Segmented African lithosphere beneath the Anatolian region inferred from teleseismic P-wave tomography. *Geophysical Journal International*, *184*(3), 1037–1057. https://doi.org/10.1111/j.1365-246X.2010.04910.x

Bikçe, M. (2016). A database for fatalities and damages due to the earthquakes in Turkey (1900–2014). *Natural Hazards*, *83*(3), 1359–1418. https://doi.org/10.1007/s11069-016-2397-7

Bilham, R., Ozener, H., Mencin, D., Dogru, A., Ergintav, S., Cakir, Z., et al. (2016). Surface creep on the North Anatolian fault at Ismetpasa, Turkey, 1944–2016. *Journal of Geophysical Research: Solid Earth*, *121*(10), 7409–7431. https://doi.org/10.1002/2016JB013394

Bird, P., Jackson, D. D., Kagan, Y. Y., Kreemer, C., & Stein, R. S. (2015). GEAR1: A global earthquake activity rate model constructed from geodetic strain rates and smoothed seismicity. *Bulletin of the Seismological Society of America*, *105*(5), 2538–2554. https://doi.org/10.1785/0120150058

Bird, P., Kreemer, C., & Holt, W. E. (2010). A long-term forecast of shallow seismicity based on the global strain rate map. *Seismological Research Letters*, *81*(2), 184–194. https://doi.org/10.1785/gssrl.81.2.184

Bird, P., & Liu, Z. (2007). Seismic hazard inferred from tectonics: California. *Seismological Research Letters*, *78*(1), 37–48. https://doi.org/10.1785/gssrl.78.1.37

Bletery, Q., Cavalié, O., Nocquet, J., & Ragon, T. (2020). Distribution of interseismic coupling along the north and East anatolian faults inferred from InSAR and GPS data. *Geophysical Research Letters*, *47*(16), e2020GL087775. https://doi.org/10.1029/2020GL087775

Bozkurt, E. (2001). Neotectonics of Turkey – A synthesis. *Geodinamica Acta*, *14*(1–3), 3–30. https://doi.org/10.1080/09853111.2001.11432432

Burc Oral, M., Reilinger, R. E., Nafi Toksöz, M., King, R. W., Aykut Barka, A., Kinik, I., & Lenk, O. (1995). Global Positioning system offers evidence of plate motions in eastern Mediterranean. *Eos, Transactions American Geophysical Union*, *76*(2), 9–11. https://doi.org/10.1029/EO076i002p00009-01

Çakir, Z., Doğan, U., Akoğlu, A. M., Ergintav, S., Özarpacı, S., Özdemir, A., et al. (2023). Arrest of the Mw 6.8 January 24, 2020 Elaziğ (Turkey) earthquake by shallow fault creep. *Earth and Planetary Science Letters*, *608*, 118085. https://doi.org/10.1016/j.epsl.2023.118085

Cavalié, O., & Jónsson, S. (2014). Block-like plate movements in eastern Anatolia observed by InSAR. *Geophysical Research Letters*, *41*(1), 26–31. https://doi.org/10.1002/2013GL058170

Cunningham, W. D., & Mann, P. (2007). Tectonics of strike-slip restraining and releasing bends. *Geological Society*, *290*(1), 1–12. https://doi.org/10.1144/SP290.1

Daout, S., Barbot, S., Peltzer, G., Doin, M.-P., Liu, Z., & Jolivet, R. (2016). Constrzaining the kinematics of metropolitan Los Angeles faults with a slip-partitioning model. *Geophysical Research Letters*, *43*(21). https://doi.org/10.1002/2016GL071061

Dewey, J. F., & Şengör, A. M. C. (1979). Aegean and surrounding regions: Complex multiplate and continuum tectonics in a convergent zone. *Geological Society of America Bulletin*, *90*(1), 84. https://doi.org/10.1130/0016-7606(1979)90<84:AASRCM>2.0.CO;2

Diercks, M., Hussain, E., Mildon, Z. K., Boulton, S. J., & Lazecký, M. (2024). Active deformation across the Western anatolian extensional Province (Türkiye) from Sentinel-1 InSAR. *Tectonics*, *43*(11), e2023TC008086. https://doi.org/10.1029/2023TC008086

Djamour, Y., Vernant, P., Nankali, H. R., & Tavakoli, F. (2011). NW Iran-eastern Turkey present-day kinematics: Results from the Iranian permanent GPS network. *Earth and Planetary Science Letters*, *307*(1–2), 27–34. https://doi.org/10.1016/j.epsl.2011.04.029

Duman, T. Y., & Emre, Ö. (2013). The East Anatolian fault: Geometry, segmentation and jog characteristics. *Geological Society*, *372*(1), 495–529. https://doi.org/10.1144/SP372.14

Elitez, İ., & Yaltırak, C. (2016). Miocene to Quaternary tectonostratigraphic evolution of the middle section of the Burdur-Fethiye shear zone, south-western Turkey: Implications for the wide inter-plate shear zones. *Tectonophysics*, *690*, 336–354. https://doi.org/10.1016/j.tecto.2016.10.003

Elitez, İ., & Yaltırak, C. (2023). Miocene to Quaternary geodynamic evolution of the southern section of the Burdur-Fethiye shear zone and its offshore continuation, eastern Mediterranean. *Tectonophysics*, *857*, 229866. https://doi.org/10.1016/j.tecto.2023.229866

Elitez, İ., Yaltırak, C., & Aktuğ, B. (2016). Extensional and compressional regime driven left-lateral shear in southwestern Anatolia (eastern Mediterranean): The Burdur-Fethiye shear zone. *Tectonophysics*, *688*, 26–35. https://doi.org/10.1016/j.tecto.2016.09.024

Emre, Ö., Duman, T., Özalp, S., Elmaci, H., Olgun, Ş., & Şaroğlu, F. (2013). *Active fault map of Turkey with an explanatory text. 1:1,250,000 scale*. General Directorate of Mineral Research and Exploration.

Emre, Ö., Duman, T., Özalp, S., Şaroğlu, F., Olgun, Ş., Elmacı, H., & Çan, T. (2018). Active fault database of Turkey. *Bulletin of Earthquake Engineering*, *16*(8), 3229–3275. https://doi.org/10.1007/s10518-016-0041-2

England, P., Houseman, G., & Nocquet, J. (2016). Constraints from GPS measurements on the dynamics of deformation in Anatolia and the Aegean. *Journal of Geophysical Research: Solid Earth*, *121*(12), 8888–8916. https://doi.org/10.1002/2016JB013382

Ergintav, S., Floyd, M., Paradissis, D., Karabulut, H., Vernant, P., Masson, F., et al. (2023). New geodetic constraints on the role of faults and blocks vs. distribute strain in the nubia-arabia-eurasia zone of active plate interactions. *Turkish Journal of Earth Sciences*, *32*(3), 248–261. https://doi.org/10.55730/1300-0985.1842

Esat, K., Seyitoğlu, G., Aktuğ, B., Kaypak, B., & Ecevitoğlu, B. (2021). The Northwest Central Anatolian Contractional Area: A neotectonic deformation zone bounded by major strike-slip fault zones in the Anatolian plate. *Tectonophysics*, *805*, 228776. https://doi.org/10.1016/j.tecto.2021.228776

Evans, E. L. (2022). A dense block model representing Western Continental United States deformation for the 2023 update to the national seismic hazard model. *Seismological Research Letters*, *93*(6), 3024–3036. https://doi.org/10.1785/0220220141

Evans, E. L., Loveless, J. P., & Meade, B. J. (2015). Total variation regularization of geodetically and geologically constrained block models for the Western United States. *Geophysical Journal International*, *202*(2), 713–727. https://doi.org/10.1093/gji/ggv164

Eyidogan, H., Güçlü, U., Utku, Z., & Degirmenci, E. (1991). *A macro-seismic guide for large earthquakes of Turkey (1900–1988)*. Kurdis Press.

Faccenna, C., Bellier, O., Martinod, J., Piromallo, C., & Regard, V. (2006). Slab detachment beneath eastern Anatolia: A possible cause for the formation of the North Anatolian fault. *Earth and Planetary Science Letters*, *242*(1–2), 85–97. https://doi.org/10.1016/j.epsl.2005.11.046

Gardner, J. K., & Knopoff, L. (1974). Is the sequence of earthquakes in Southern California, with aftershocks removed, Poissonian? *Bulletin of the Seismological Society of America*, *64*(5), 1363–1367. https://doi.org/10.1785/BSSA0640051363

Gasperini, L., Polonia, A., Çağatay, M. N., Bortoluzzi, G., & Ferrante, V. (2011). Geological slip rates along the North Anatolian fault in the Marmara region. *Tectonics*, *30*(6), 2011TC002906. https://doi.org/10.1029/2011TC002906

Gezgin, C., Ekercin, S., Ibrahim, T., Aktuğ, B., Erdoğan, H., Gürbüz, E., et al. (2022). Determination of recent tectonic deformations along the Tuz Gölü Fault zone in Central Anatolia (Turkey) with GNSS observations. *Turkish Journal of Earth Sciences*, *31*(1), 20–33. https://doi.org/10.3906/yer-2108-10

Grant, M., & Boyd, S. (2008). Graph implementations for nonsmooth convex programs, Recent advances in learning and control (A tribute to M. Vidyasagar). In V. Blondel, S. Boyd, & H. Kimura (Eds), *Lecture notes in control and information sciences*. Springer

Grant, M., & Boyd, S. (2013). CVX: Matlab software for disciplined convex programming, version 2.0 beta. Retrieved from http://cvxr.com/cvx

Gülerce, Z., Tanvir Shah, S., Menekşe, A., Arda Özacar, A., Kaymakci, N., & Önder Çetin, K. (2017). Probabilistic seismic-hazard assessment for East Anatolian fault zone using planar fault source models. *Bulletin of the Seismological Society of America*, *107*(5), 2353–2366. https://doi.org/10.1785/0120170009

Hammond, W. C., Kreemer, C., & Blewitt, G. (2024). Robust imaging of fault slip rates in the walker Lane and Western great Basin from GPS data using a multi-block model approach. *Journal of Geophysical Research: Solid Earth*, *129*(3), e2023JB028044. https://doi.org/10.1029/2023JB028044

Hanks, T. C., & Kanamori, H. (1979). A moment magnitude scale. *Journal of Geophysical Research*, *84*(B5), 2348–2350. https://doi.org/10.1029/JB084iB05p02348

Hayes, G. P., Moore, G. L., Portner, D. E., Hearne, M., Flamme, H., Furtney, M., & Smoczyk, G. M. (2018). Slab2, a comprehensive subduction zone geometry model. *Science*, *362*(6410), 58–61. https://doi.org/10.1126/science.aat4723

He, L., Feng, G., Xu, W., Wang, Y., Xiong, Z., Gao, H., & Liu, X. (2023). Coseismic kinematics of the 2023 Kahramanmaras, Turkey earthquake sequence from InSAR and optical data. *Geophysical Research Letters*, *50*(17), e2023GL104693. https://doi.org/10.1029/2023GL104693

Hempton, M. R. (1987). Constraints on arabian plate motion and extensional history of the Red Sea. *Tectonics*, *6*(6), 687–705. https://doi.org/10.1029/TC006i006p00687

Huang, M.-H., & Evans, E. L. (2019). Total variation regularization of geodetically constrained block models in Southwest Taiwan. *Journal of Geophysical Research: Solid Earth*, *124*(12), 13269–13285. https://doi.org/10.1029/2019JB018076

Hubert-Ferrari, A., Armijo, R., King, G., Meyer, B., & Barka, A. (2002). Morphology, displacement, and slip rates along the North Anatolian fault, Turkey. *Journal of Geophysical Research*, *107*(B10). https://doi.org/10.1029/2001JB000393

Hussain, E., Wright, T. J., Walters, R. J., Bekaert, D., Hooper, A., & Houseman, G. A. (2016). Geodetic observations of postseismic creep in the decade after the 1999 Izmit earthquake, Turkey: Implications for a shallow slip deficit. *Journal of Geophysical Research: Solid Earth*, *121*(4), 2980–3001. https://doi.org/10.1002/2015JB012737

Hussain, E., Wright, T. J., Walters, R. J., Bekaert, D. P. S., Lloyd, R., & Hooper, A. (2018). Constant strain accumulation rate between major earthquakes on the North Anatolian fault. *Nature Communications*, *9*(1), 1392. https://doi.org/10.1038/s41467-018-03739-2

Jia, Z., Jin, Z., Marchandon, M., Ulrich, T., Gabriel, A.-A., Fan, W., et al. (2023). The complex dynamics of the 2023 Kahramanmaraş, Turkey, Mw 7.8-7.7 earthquake doublet. *Science*, *381*(6661), 985–990. https://doi.org/10.1126/science.adi0685

Jolivet, R., Jara, J., Dalaison, M., Rouet-Leduc, B., Ozdemir, A., Dogan, U., et al. (2023). Daily to Centennial behavior of aseismic slip along the central section of the north Anatolian fault. *Journal of Geophysical Research: Solid Earth*, *128*(7), e2022JB026018. https://doi.org/10.1029/2022JB026018

Karakhanyan, A., Vernant, P., Doerflinger, E., Avagyan, A., Philip, H., Aslanyan, R., et al. (2013). GPS constraints on continental deformation in the Armenian region and Lesser Caucasus. *Tectonophysics*, *592*, 39–45. https://doi.org/10.1016/j.tecto.2013.02.002

Kreemer, C., Blewitt, G., & Klein, E. C. (2014). A geodetic plate motion and Global strain rate model. *Geochemistry, Geophysics, Geosystems*, *15*(10), 3849–3889. https://doi.org/10.1002/2014GC005407

Kurt, A. I., Ozbakir, A. D., CiNgoz, A., Ergintav, S., Dogan, U., & Ozarpaci, S. (2023). Contemporary velocity field for Turkey inferred from combination of a dense network of long term GNSS observations. *Turkish Journal of Earth Sciences*, *32*(3), 275–293. https://doi.org/10.55730/1300-0985.1844

Kurt, H., Sorlien, C. C., Seeber, L., Steckler, M. S., Shillington, D. J., Cifci, G., et al. (2013). Steady late quaternary slip rate on the Cinarcik section of the North Anatolian fault near Istanbul, Turkey. *Geophysical Research Letters*, *40*(17), 4555–4559. https://doi.org/10.1002/grl.50882

McClusky, S., Balassanian, S., Barka, A., Demir, C., Ergintav, S., Georgiev, I., et al. (2000). Global positioning system constraints on plate kinematics and dynamics in the eastern Mediterranean and Caucasus. *Journal of Geophysical Research*, *105*(B3), 5695–5719. https://doi.org/10.1029/1999JB900351

McKenzie, D. P. (1970). Plate tectonics of the Mediterranean Region. *Nature*, *226*(5242), 239–243. https://doi.org/10.1038/226239a0

McKenzie, D. P. (1972). Active tectonics of the Mediterranean Region. *Geophysical Journal International*, *30*(2), 109–185. https://doi.org/10.1111/j.1365-246X.1972.tb02351.x

Meade, B. J., & Loveless, J. P. (2009). Block modeling with connected fault-network geometries and a Linear elastic coupling estimator in spherical coordinates. *Bulletin of the Seismological Society of America*, *99*(6), 3124–3139. https://doi.org/10.1785/0120090088

Mozafari, N., Tikhomirov, D., Sumer, Ö., Özkaymak, Ç., Uzel, B., Yeşilyurt, S., et al. (2019). Dating of active normal fault scarps in the Büyük Menderes Graben (western Anatolia) and its implications for seismic history. *Quaternary Science Reviews*, *220*, 111–123. https://doi.org/10.1016/j.quascirev.2019.07.002

Nissen, E., Cambaz, M. D., Gaudreau, É., Howell, A., Karasözen, E., & Savidge, E. (2022). A reappraisal of active tectonics along the Fethiye-Burdur trend, southwestern Turkey. *Geophysical Journal International*, *230*(2), 1030–1051. https://doi.org/10.1093/gji/ggac096

Nyst, M., & Thatcher, W. (2004). New constraints on the active tectonic deformation of the Aegean. *Journal of Geophysical Research*, *109*(B11), 2003JB002830. https://doi.org/10.1029/2003JB002830

Okada, Y. (1985). Surface deformation due to shear and tensile faults in a half-space. *Bulletin of the Seismological Society of America*, *75*(4), 1135–1154. https://doi.org/10.1785/BSSA0750041135

Özbakır, A. D., Şengör, A. M. C., Wortel, M. J. R., & Govers, R. (2013). The Pliny-Strabo trench region: A large shear zone resulting from slab tearing. *Earth and Planetary Science Letters*, *375*, 188–195. https://doi.org/10.1016/j.epsl.2013.05.025

Özbey, V., Özeren, M. S., Henry, P., Klein, E., Galgana, G., Karabulut, H., et al. (2021). Kinematics of the Marmara Region: A fusion of continuum and block models. *Mediterranean Geoscience Reviews*, *3*(1), 57–78. https://doi.org/10.1007/s42990-021-00051-y

Özbey, V., Sengör, A. M. C., Henry, P., Özeren, M. S., Haines, A. J., Klein, E. C., et al. (2024). Kinematics of the Kahramanmaraş triple junction and of Cyprus: Evidence of shear partitioning. *Bulletin de la Societe Geologique de France*, *195*(1), 15. https://doi.org/10.1051/bsgf/2024012

Özkan, A., Yavaşoğlu, H. H., & Masson, F. (2023). Present-day strain accumulations and fault kinematics at the Hatay Triple Junction using new geodetic constraints. *Tectonophysics*, *854*, 229819. https://doi.org/10.1016/j.tecto.2023.229819

Reilinger, R. E., McClusky, S. C., Oral, M. B., King, R. W., Toksoz, M. N., Barka, A. A., et al. (1997). Global positioning system measurements of present-day crustal movements in the Arabia-Africa-Eurasia plate collision zone. *Journal of Geophysical Research*, *102*(B5), 9983–9999. https://doi.org/10.1029/96JB03736

Reilinger, R. E., McClusky, S. C., Vernant, P., Lawrence, S., Ergintav, S., Cakmak, R., et al. (2006). GPS constraints on continental deformation in the Africa-Arabia-Eurasia continental collision zone and implications for the dynamics of plate interactions. *Journal of Geophysical Research*, *111*(B5), 2005JB004051. https://doi.org/10.1029/2005JB004051

Reitman, N. G., Briggs, R. W., Barnhart, W. D., Hatem, A. E., Thompson Jobe, J. A., DuRoss, C. B., et al. (2023). Rapid surface rupture mapping from satellite data: The 2023 Kahramanmaraş, Turkey (Türkiye), earthquake sequence. *The Seismic Record*, *3*(4), 289–298. https://doi.org/10.1785/0320230029

Şahin, M., Yaltırak, C., & Karacık, Z. (2019). A case study of compression to escape tectonic transition: Tectonic evolution of the Nallıhan Wedge and comparison with the Tercan Wedge (Eastern Mediterranean, Turkey). *Journal of Asian Earth Sciences*, *174*, 311–331. https://doi.org/10.1016/j.jseaes.2018.12.016

Sançar, T., Zabcı, C., Akçar, N., Karabacak, V., Yeşilyurt, S., Yazıcı, M., et al. (2020). Geodynamic importance of the strike-slip faults at the eastern part of the Anatolian Scholle: Inferences from the uplift and slip rate of the Malatya Fault (Malatya-Ovacık fault zone, eastern Turkey). *Journal of Asian Earth Sciences*, *188*, 104091. https://doi.org/10.1016/j.jseaes.2019.104091

Santamaría-Gómez, A., Bouin, M.-N., Collilieux, X., & Wöppelmann, G. (2011). Correlated errors in GPS position time series: Implications for velocity estimates. *Journal of Geophysical Research*, *116*(B1), B01405. https://doi.org/10.1029/2010JB007701

Savage, J. C., & Simpson, R. W. (1997). Surface strain accumulation and the seismic moment tensor. *Bulletin of the Seismological Society of America*, *87*(5), 1345–1353. https://doi.org/10.1785/BSSA0870051345

Selçuk, A. S., Erturaç, M. K., & Nomade, S. (2016). Geology of the Çaldıran Fault, Eastern Turkey: Age, slip rate and implications on the characteristic slip behaviour. *Tectonophysics*, *680*, 155–173. https://doi.org/10.1016/j.tecto.2016.05.019

Şengör, A. M. C. (1979). The North Anatolian transform fault: Its age, offset and tectonic significance. *Journal of the Geological Society*, *136*(3), 269–282. https://doi.org/10.1144/gsjgs.136.3.0269

Şengör, A. M. C., Tüysüz, O., İmren, C., Sakınç, M., Eyidoğan, H., Görür, N., et al. (2005). The North Anatolian fault: A new look. *Annual Review of Earth and Planetary Sciences*, *33*(1), 37–112. https://doi.org/10.1146/annurev.earth.32.101802.120415

Seyitoglu, G., Ecevitoglu, G. B., Kaypak, B., Guney, Y., Tun, M., Esat, K., & Uyar Aldaş, G. (2015). Determining the main strand of the Eskişehir strike-slip fault zone using subsidiary structures and seismicity: A hypothesis tested by seismic reflection studies. *Turkish Journal of Earth Sciences*, *24*, 1–20. https://doi.org/10.3906/yer-1406-5

Seyitoglu, G., Aktug, B., Esat, K., & Kaypak, B. (2022a). Neotectonics of Turkey (Türkiye) and surrounding regions: A new perspective with block modelling. *Geológica Acta*, *20*, 1–21. https://doi.org/10.1344/GeologicaActa2022.20.4

Seyitoglu, G., Tuncel, E., Kaypak, B., Esat, K., & Gokkaya, E. (2022b). The Anatolian diagonal: A broad left lateral shear zone between the North Anatolian fault zone and the Aegean/Cyprus arcs. *Geological Bulletin of Turkey*, *65*, 93–116. https://doi.org/10.25288/tjb.1015537

Shen, Z., & Bird, P. (2022). NeoKinema deformation model for the 2023 update to the U.S. national seismic hazard model. *Seismological Research Letters*, *93*(6), 3037–3052. https://doi.org/10.1785/0220220179

Shen, Z., Wang, M., Zeng, Y., & Wang, F. (2015). Optimal interpolation of spatially discretized geodetic data. *Bulletin of the Seismological Society of America*, *105*(4), 2117–2127. https://doi.org/10.1785/0120140247

Simão, N. M., Nalbant, S. S., Sunbul, F., & Komec Mutlu, A. (2016). Central and eastern Anatolian crustal deformation rate and velocity fields derived from GPS and earthquake data. *Earth and Planetary Science Letters*, *433*, 89–98. https://doi.org/10.1016/j.epsl.2015.10.041

Solak, H. İ., Tiryakioğlu, İ., Özkaymak, Ç., Sözbilir, H., Aktuğ, B., Yavaşoğlu, H. H., & Özkan, A. (2024). Recent tectonic features of Western Anatolia based on half-space modeling of GNSS data. *Tectonophysics*, *872*, 230194. https://doi.org/10.1016/j.tecto.2023.230194

Straub, C., & Kahle, H.-G. (1994). Global positioning system (GPS) estimates of crustal deformation in the Marmara Sea region, Northwestern Anatolia. *Earth and Planetary Science Letters*, *121*(3), 495–502. https://doi.org/10.1016/0012-821X(94)90086-8

Stucchi, M., Rovida, A., Gomez Capera, A. A., Alexandre, P., Camelbeeck, T., Demircioglu, M. B., et al. (2013). The SHARE European earthquake catalogue (SHEEC) 1000–1899. *Journal of Seismology*, *17*(2), 523–544. https://doi.org/10.1007/s10950-012-9335-2

Sun, K. (2025). GNSS velocity field and earthquake catalog in Turkiye (v2) [Dataset]. *Zenodo*. https://doi.org/10.5281/zenodo.19501626

Tan, O. (2021). A homogeneous earthquake catalogue for Turkey. *Natural Hazards and Earth System Sciences*, *21*(7), 2059–2073. https://doi.org/10.5194/nhess-21-2059-2021

Tan, O., Tapirdamaz, M. C., & Yörük, A. (2008). The earthquake catalogues for Turkey. *Turkish Journal of Earth Sciences*, *17*, 405–418.

Temiz, H., Guezou, J. C., Tatar, O., Unlügenç, U. C., & Poisson, A. (2002). Tectonostratigraphy of the Tercan-Çayirli Basin: Implications for the Neogene-Quaternary tectonic deformation of the Northeast anatolian block, Turkey. *International Geology Review*, *44*(3), 243–253. https://doi.org/10.2747/0020-6814.44.3.243

Tiryakioğlu, İ., Floyd, M., Erdoğan, S., Gülal, E., Ergintav, S., McClusky, S., & Reilinger, R. (2013). GPS constraints on active deformation in the Isparta Angle region of SW Turkey. *Geophysical Journal International*, *195*(3), 1455–1463. https://doi.org/10.1093/gji/ggt323

Van Hinsbergen, D. J. J., Maffione, M., Plunder, A., Kaymakcı, N., Ganerød, M., Hendriks, B. W. H., et al. (2016). Tectonic evolution and paleogeography of the Kırşehir Block and the central anatolian Ophiolites, Turkey: Tectonic evolution of central Anatolia. *Tectonics*, *35*(4), 983–1014. https://doi.org/10.1002/2015TC004018

Walters, R. J., Parsons, B., & Wright, T. J. (2014). Constraining crustal velocity fields with InSAR for Eastern Turkey: Limits to the block-like behavior of Eastern Anatolia. *Journal of Geophysical Research: Solid Earth*, *119*(6), 5215–5234. https://doi.org/10.1002/2013JB010909

Wang, W., Qiao, X., & Ding, K. (2021). Present-day kinematics in Southeastern Tibet inferred from GPS measurements. *Journal of Geophysical Research: Solid Earth*, *126*(1), e2020JB021305. https://doi.org/10.1029/2020JB021305

Wang, W., Zhao, B., Qiao, X., & Ding, K. (2022). Block kinematics in North China from GPS measurements. *Geochemistry, Geophysics, Geosystems*, *23*(3), e2021GC010216. https://doi.org/10.1029/2021GC010216

Weiss, J. R., Walters, R. J., Morishita, Y., Wright, T. J., Lazecky, M., Wang, H., et al. (2020). High-resolution surface velocities and strain for Anatolia from Sentinel-1 InSAR and GNSS data. *Geophysical Research Letters*, *47*(17), e2020GL087376. https://doi.org/10.1029/2020GL087376

Wessel, P., Luis, J. F., Uieda, L., Scharroo, R., Wobbe, F., Smith, W. H. F., & Tian, D. (2019). The generic mapping tools version 6. *Geochemistry, Geophysics, Geosystems*, *20*(11), 5556–5564. https://doi.org/10.1029/2019GC008515

Whitney, D. L., Delph, J. R., Thomson, S. N., Beck, S. L., Brocard, G. Y., Cosca, M. A., et al. (2023). Breaking plates: Creation of the East Anatolian fault, the Anatolian plate, and a tectonic escape system. *Geology*, *51*(7), 673–677. https://doi.org/10.1130/G51211.1

Williams, S. D. P., Bock, Y., Fang, P., Jamason, P., Nikolaidis, R. M., Prawirodirdjo, L., et al. (2004). Error analysis of continuous GPS position time series. *Journal of Geophysical Research*, *109*(B3). https://doi.org/10.1029/2003JB002741

Yıldırım, C., Sarıkaya, M. A., & Çiner, A. (2016). Late Pleistocene intraplate extension of the Central Anatolian Plateau, Turkey: Inferences from cosmogenic exposure dating of alluvial fan, landslide, and moraine surfaces along the Ecemiş fault zone. *Tectonics*, *35*(6), 1446–1464. https://doi.org/10.1002/2015TC004038

Yolsal-Çevikbilen, S., Taymaz, T., & Helvacı, C. (2014). Earthquake mechanisms in the Gulfs of Gökova, Sığacık, Kuşadası, and the Simav Region (western Turkey): Neotectonics, seismotectonics and geodynamic implications. *Tectonophysics*, *635*, 100–124. https://doi.org/10.1016/j.tecto.2014.05.001

Yönlü, Ö., Altunel, E., & Karabacak, V. (2017). Geological and geomorphological evidence for the southwestern extension of the East Anatolian fault zone, Turkey. *Earth and Planetary Science Letters*, *469*, 1–14. https://doi.org/10.1016/j.epsl.2017.03.034

Zelenin, E., Bachmanov, D., Garipova, S., Trifonov, V., & Kozhurin, A. (2022). The active faults of Eurasia Database (AFEAD): The ontology and design behind the continental-scale dataset. *Earth System Science Data*, *14*(10), 4489–4503. https://doi.org/10.5194/essd-14-4489-2022

Zhao, G., Meng, G., Wu, W., Su, X., & Pan, Z. (2022). Earthquake potential assessment around the Southeastern Tibetan Plateau based on seismic and geodetic data. *Pure and Applied Geophysics*, *179*(1), 11–44. https://doi.org/10.1007/s00024-021-02917-6